Inclusive rates from smeared spectral functions in the two-dimensional O(3) non-linear σ-model

John Bulava,[1,*] Maxwell T. Hansen,[2,†] Michael W. Hansen,[3,‡] Agostino Patella,[4,§] and Nazario Tantalo[5,¶]

[1] *Deutsches Elektronen-Synchrotron DESY Platanenallee 6, 15738 Zeuthen, Germany*
[2] *Higgs Centre for Theoretical Physics, School of Physics and Astronomy, The University of Edinburgh, Edinburgh EH9 3FD, UK*
[3] *University of Graz, Institute for Physics, A-8010 Graz, Austria*
[4] *Institut für Physik und IRIS Adlershof, Humboldt-Universität zu Berlin, Zum Großen Windkanal 6, D-12489 Berlin, Germany*
[5] *University and INFN of Roma Tor Vergata, Via della Ricerca Scientifica 1, I-00133, Rome, Italy*

(Dated: November 17, 2021)

This work employs the spectral reconstruction approach of Ref. [1] to determine an inclusive rate in the $1+1$ dimensional O(3) non-linear σ-model, analogous to the QCD part of $e^+e^- \to$ hadrons. The Euclidean two-point temporal correlation function of the conserved current j is computed using Monte Carlo lattice field theory simulations for a variety of spacetime volumes and lattice spacings. The spectral density of this correlator is related to the inclusive rate for $j \to \mathrm{X}$ in which all final states produced by the external current are summed. The ill-posed inverse problem of determining the spectral density via the Euclidean correlator is made tractable using smeared spectral functions in which the underlying target function is convolved with a set of known smearing kernels of finite width ϵ. The smooth energy dependence of the desired spectral function enables a controlled $\epsilon \to 0$ extrapolation in the inelastic region, yielding the real-time inclusive rate *without* reference to individual finite-volume energies or matrix elements. Systematic uncertainties due cutoff effects, finite-volume effects, and the reconstruction algorithm are estimated and taken into account in the final error budget. After taking the continuum limit, the results are consistent with the known analytic rate to within the combined statistical and systematic errors. Above energies where 20-particle states contribute, the statistical precision is sufficient to discern four-particle contributions to the spectral function.

* john.bulava@desy.de
† maxwell.hansen@ed.ac.uk
‡ michael.hansen@uni-graz.at
§ agostino.patella@physik.hu-berlin.de
¶ nazario.tantalo@roma2.infn.it

CONTENTS

I. INTRODUCTION

Markov chain Monte Carlo simulations of lattice QCD continue to provide a quantitative window into the strong nuclear force. However, the Euclidean metric signature required for the Monte Carlo solution of QCD path integrals complicates the study of real-time scattering processes. Although the spatial volume dependence of energies and matrix elements has successfully been used as a probe of few-particle scattering amplitudes [2], this approach is inapplicable to energies above arbitrary multi-particle thresholds and is restricted to center-of-mass energies corresponding to finite-volume spatial momenta. This last disadvantage hampers the continuum limit of amplitudes at fixed energy, which can only be achieved by maintaining a constant physical volume as the lattice spacing is decreased. The straightforward determination of inclusive rates is also difficult using the finite-volume formalism.

An alternative approach [3] is to use Euclidean correlation functions computed in lattice simulations to determine spectral densities which are independent of the metric signature. This approach is not subject to the same limitations as finite-volume methods and has been fully developed for inclusive amplitudes mediated by an external current [4] as well as arbitrary scattering processes [5, 6][1]. A major obstacle of this program is the solution of an ill-posed inverse problem to determine continuous spectral densities from correlation functions at a finite set of time separations with statistical errors. In Refs. [9, 10] Backus and Gilbert deal with this by instead computing spectral functions smeared with a kernel that is known *a posteriori*. An important advancement by Refs. [1, 11] enables the smearing kernel to be specified *a priori*.

Although these methods are not new, their application to compute scattering amplitudes from actual Monte Carlo simulation data, with a detailed analysis of both statistical and systematic errors, has not yet been performed. It is therefore worthwhile to perform such a test in a controlled setting. This work employs the spectral reconstruction strategy of Ref. [1] to determine an inclusive rate in the two-dimensional O(3) non-linear σ-model. As in Ref. [12], comparison is made with exact continuum results. However, our work overcomes the limitations mentioned above: the inclusive rate is computed above inelastic thresholds and the continuum limit is taken at fixed center-of-mass energy without the need for a constant physical volume. Large physical simulation volumes are however required to control finite-volume effects in the smeared spectral functions at fixed smearing width. After ensuring that finite-size and cutoff effects are under control, the desired spectral function is obtained by extrapolating the smearing width to zero.

For this first application we treat a process akin to $e^+e^- \to$ hadrons, the QCD component of which is given by the spectral function

$$\rho_{\mu\nu}(k) = \frac{1}{2\pi}\int d^4x\, e^{-ik\cdot x}\langle\Omega|\hat{j}^{\rm em}_\mu(x)\,\hat{j}^{\rm em}_\nu(0)|\Omega\rangle = (g_{\mu\nu}k^2 - k_\mu k_\nu)\,\rho(k^2), \tag{1}$$

where the integral is performed in Minkowski space, $\hat{j}^{\rm em}_\mu$ is the quark-level electromagnetic current and the relation to the physical process is

$$\rho(s) = \frac{R(s)}{12\pi^2}, \quad R(s) = \frac{\sigma\left[e^+e^- \to \text{hadrons}\right](s)}{4\pi\alpha_{\rm em}(s)^2/(3s)}. \tag{2}$$

This celebrated 'R-ratio' has a number of phenomenological applications including the hadronic vacuum polarization contribution to the anomalous magnetic moment of the muon. It can be obtained via spectral reconstruction of the Euclidean correlator in the time-momentum representation

$$C(t) = -\int d^3\boldsymbol{x}\,\langle\Omega|\hat{j}^{\rm em}_z(\boldsymbol{x})\,e^{-\hat{H}t}\,\hat{j}^{\rm em}_z(0)|\Omega\rangle = \int_0^\infty d\omega\,\omega^2\rho(\omega^2)\,e^{-\omega t} \tag{3}$$

computed in lattice QCD simulations. Everything discussed here is readily transferrable to the lattice determination of $\rho(s)$ from $C(t)$ in QCD. While computations of $\rho(s)$ are naturally compared with experimental determinations of $R(s)$, numerical results for the spectral density computed here are compared with the corresponding analytical predictions in Fig. 9, which is the main result of this work.

This work is organized as follows. Sec. II defines the spectral function of interest in the O(3)-model, outlines the reconstruction approach, and suggests a strategy for extrapolating the smearing width to zero. Sec. III discusses the influence of the finite torus on which the simulations are performed while Sec. IV defines the lattice regularization and discusses the continuum limit. Sec. V presents numerical results and Sec. VI concludes.

---

[1] For the application of spectral-density methods to inclusive semi-leptonic B-meson decay rates see Refs. [7, 8].

II. GENERAL FRAMEWORK IN CONTINUOUS INFINITE VOLUME

This section introduces the two-dimensional O(3) non-linear σ-model and the Euclidean correlator $C(t)$ with spectral function $\rho(\omega)$, which are both defined via the conserved vector current. We additionally review the algorithm of Ref. [1] for systematically determining a smeared version of $\rho(\omega)$ from numerical estimates of $C(t)$ and detail an extrapolation procedure for taking the smearing width to zero. In this section the Euclidean spacetime is assumed to be continuous and infinite in both directions. Peculiarities due to the torus are discussed in Sec. III and the lattice discretization in Sec. IV.

The continuum Euclidean action of the 2-dimensional O(3)-model is defined as

$$S[\sigma] = \frac{1}{2g^2} \int d^2x \, \partial_\mu \sigma(x) \cdot \partial_\mu \sigma(x) \,, \tag{4}$$

where the 3-component real field $\sigma^a(x)$ has unit length $\sigma(x) \cdot \sigma(x) = 1$. The O(3)-model is asymptotically free, has a dynamically-generated mass gap m, and is integrable. It also possesses a global O(3) symmetry which rotates the field $\sigma(x)$. The corresponding Noether current is given by

$$j^c_\mu(x) = \frac{1}{g^2} \epsilon^{abc} \sigma^a(x) \partial_\mu \sigma^b(x) \,, \tag{5}$$

where ϵ^{abc} is the Levi-Civita tensor and repeated indices are summed. This current transforms irreducibly under the $I = 1$ (fundamental) representation of O(3).

The aim of this work is to reconstruct the spectral function $\rho(\omega)$ associated with j^c_μ from Euclidean correlation functions determined numerically from lattice Monte Carlo simulations. The spectral function is defined implicitly via the relation

$$2\pi \, \langle \Omega | \hat{j}^a_\mu(0) \, \delta^2(\hat{P} - p) \, \hat{j}^b_\nu(0) | \Omega \rangle = \frac{\delta^{ab}}{3} \left(\delta_{\mu\nu} - \frac{p_\mu p_\nu}{p^2} \right) \rho\left(\sqrt{p^2} \right) \,, \tag{6}$$

where $\hat{P} = (\hat{H}, \hat{\boldsymbol{P}})$ is the 2-momentum operator with eigenvalues $p = (E, \boldsymbol{p})$. We have used covariance under the O(3) internal symmetry and the Euclidean spacetime SO(2) symmetry as well as current conservation to factorize the function $\rho\left(\sqrt{p^2}\right)$. By specializing the above relation to $\mu = \nu = 1$ and $p = (E, 0)$, and contracting the internal indices, one obtains the more direct definition

$$\rho(E) = 2\pi \, \langle \Omega | \hat{j}^a_1(0) \, \delta^2(\hat{P} - p) \, \hat{j}^a_1(0) | \Omega \rangle \,. \tag{7}$$

The utility of the 2-dimensional O(3)-model for the present study is that (due to integrability) $\rho(E)$ can be computed analytically, enabling a comparison between our numerical reconstruction and the exact result. The spectral function decomposes into sectors defined by the number n of asymptotic particles[2] propagating between the two currents

$$\rho(E) = \sum_{\text{even } n \geq 2} \rho^{(n)}(E) \,. \tag{8}$$

The contribution $\rho^{(n)}(E)$ has support for $E > n\,m$, where m is the mass gap. Even though integrability (together with a number of mild and generally accepted assumptions) fixes $\rho^{(n)}(E)$ for every even value of n, explicit expressions have been worked out only for $n = 2, 4, 6$. At the energies considered in this work the sum over the number of particles is rapidly convergent and the $n = 6$ contribution is at least a couple of orders of magnitude smaller than the $n = 4$ contribution. In the following we therefore refer to the spectral function summed over $n = 2, 4, 6$ as the *exact spectral function*. The $n = 2$ contribution can be written in closed form

$$\rho^{(2)}(E) = \frac{3\pi^3}{8\theta^2} \, \frac{\theta^2 + \pi^2}{\theta^2 + 4\pi^2} \, \tanh^3 \frac{\theta}{2} \, \Bigg|_{\theta = 2 \cosh^{-1} \frac{E}{2m}} \tag{9}$$

while the $n = 4, 6$ contributions are expressed in terms of phase-space integrals that require numerical evaluation as discussed in App. A.

---

[2] The n-particle states interpolated by the current of course also transform irreducibly under the $I = 1$ representation of O(3).

This spectral function is related to the Euclidean-signature current-current correlator at zero spatial momentum via the Laplace transform

$$C(t) \equiv \int d\boldsymbol{x}\, \langle \Omega |\, \hat{j}_1^a(0,\boldsymbol{x})\, e^{-\hat{H}t}\, \hat{j}_1^a(0)\, |\Omega\rangle = \int_0^\infty d\omega\, e^{-\omega t}\, \rho(\omega)\,. \tag{10}$$

The demonstration of a systematic method to invert this relation, given realistic numerical estimates of $C(t)$ at a finite set of time slices with statistical errors, is the central focus of this work.

As described for example in Ref. [13], the inverse Laplace transform is numerically ill-conditioned. A promising way forward is to recognize that $\rho(\omega)$ is not directly extractable from numerical data and that one should instead target the smeared spectral function

$$\rho_\epsilon(E) = \int_0^\infty d\omega\, \delta_\epsilon(E,\omega)\, \rho(\omega)\,, \tag{11}$$

where $\delta_\epsilon(E,\omega)$ is any approximation of the Dirac δ-function satisfying $\lim_{\epsilon\to 0} \delta_\epsilon(E,\omega) = \delta(E-\omega)$ and $\int_{-\infty}^{\infty} d\omega\, \delta_\epsilon(E,\omega) = 1$. The challenge of recovering $\rho_\epsilon(E)$ from $C(t)$ can then be made arbitrarily mild (or severe) by varying the specific functional form of $\delta_\epsilon(E,\omega)$ and the values of ϵ and E.

Following Ref. [1] we consider smearing kernels $\delta_\epsilon(E,\omega)$ that can be represented exactly as

$$\delta_\epsilon(E,\omega) = a \sum_{\tau=1}^{\infty} g_\tau^{\text{target}}\, b_\tau(\omega)\,, \tag{12}$$

where τ is a dimensionless integer variable, a an arbitrary scale with dimensions of inverse energy to be later identified with the lattice spacing, the $b_\tau(\omega)$ are basis functions, and $g_\tau^{\text{target}} \equiv g_\tau^{\text{target}}(\epsilon, E)$ coordinates that represent the target smearing function $\delta_\epsilon(E,\omega)$ in this basis. By using $b_\tau(\omega) = \mathrm{e}^{-a\omega\tau}$ the smeared spectral density is given by

$$\rho_\epsilon(E) = a \sum_{\tau=1}^{\infty} g_\tau^{\text{target}} C(a\tau) = \int_0^\infty d\omega\, \delta_\epsilon(E,\omega)\, \rho(\omega)\,. \tag{13}$$

The choice $b_\tau(\omega) = \mathrm{e}^{-a\omega\tau}$ is based on the non-essential assumption that spacetime is infinite. In practice, as explained in Sec. III, we use a basis that takes into account the periodicity of the finite temporal direction.

An estimator for $\rho_\epsilon(E)$ is obtained by approximating $\delta_\epsilon(E,\omega)$ with an element of the space spanned by a finite number of basis functions. A generic function $\Delta(\omega)$ in this space is represented as

$$\Delta(\omega) = a \sum_{\tau=1}^{\tau_{\max}} g_\tau\, b_\tau(\omega) \tag{14}$$

and the coefficients g_τ corresponding to the approximation of $\delta_\epsilon(E,\omega)$ are determined by minimizing the functional[3]

$$W_\lambda[g] = (1-\lambda)\frac{A[g]}{A[0]} + \lambda B[g]\,, \tag{15}$$

where $\lambda \in [0,1]$ is the 'trade-off' parameter (discussed shortly) and the functionals $A[g]$ and $B[g]$ are given by

$$A[g] = \int_{E_0}^\infty d\omega \left\{ \delta_\epsilon(E,\omega) - a \sum_{\tau=1}^{\tau_{\max}} g_\tau\, b_\tau(\omega) \right\}^2, \qquad B[g] = \sum_{\tau,\tau'=1}^{\tau_{\max}} g_\tau g_{\tau'}\, \mathrm{Cov}\left[aC(a\tau), aC(a\tau')\right]\,. \tag{16}$$

The relative normalization of the $A[g]$ and $B[g]$ functionals in Eq. (15) differs from Ref. [1]. The factor $1/(aC(0))^2$ in the normalization of $B[g]$ present there is not included here since $aC(0) \simeq 1$ while the factor $1/A[0]$ in the first term of Eq. (15) makes it dimensionless ($A[0] \propto 1/\epsilon$).

As discussed in App. B, $A[g]$ and $B[g]$ are both positive quadratic forms in the variables g_τ so that the minimum conditions

$$\left.\frac{\partial W_\lambda[g]}{\partial g_\tau}\right|_{g_\tau = g_\tau^\lambda} = 0 \tag{17}$$

---

[3] Possible additional constraints on the minimization are discussed in App. B.

x	w_k^{x}, even k	w_k^{x}, odd k	w_1^{x}	w_2^{x}	w_3^{x}	w_4^{x}
g	$\frac{k!}{(-2)^{k/2}(k/2)!}$	0	0	-1	0	3
c0	1	1	1	1	1	1
c1	$(1-k)$	$(1-k)$	0	-1	-2	-3
c2	$\frac{1}{3}(k-3)(k-1)$	$\frac{1}{3}(k-3)(k-1)$	0	$-1/3$	0	1

TABLE I. Summary of the coefficients w_k^{x} entering Eq. (22). It should be noted that w_3^{c1} and w_5^{c2} are the lowest non-zero coefficients with odd k for their respective smearing kernels, which is not reflected in the general formulae.

are a linear system of equations to be solved for the coefficients $g_\tau^\lambda \equiv g_\tau^\lambda(\epsilon, E, \tau_{\max})$. These coefficients define the approximation of $\delta_\epsilon(E,\omega)$ and the associated estimator for $\rho_\epsilon(E)$ according to

$$\delta_\epsilon^\lambda(E,\omega) = a\sum_{\tau=1}^{\tau_{\max}} g_\tau^\lambda\, b_\tau(\omega)\;, \qquad \rho_\epsilon^\lambda(E) = a\sum_{\tau=1}^{\tau_{\max}} g_\tau^\lambda C(a\tau) = \int_0^\infty d\omega\, \delta_\epsilon^\lambda(E,\omega)\,\rho(\omega)\;. \tag{18}$$

The functional $B[g^\lambda]$ is simply the statistical variance of $\rho_\epsilon^\lambda(E)$ and therefore vanishes in the ideal case of infinitely precise input data. On the other hand, $A[g^\lambda]$ measures the distance between the target kernel $\delta_\epsilon(E,\omega)$ and its approximation $\delta_\epsilon^\lambda(E,\omega)$ in the range[4] $E \in [E_0, \infty]$. It can only vanish in the limit $\tau_{\max} \to \infty$ when $g_\tau^\lambda \to g_\tau^{\text{target}}$. The coefficients g^λ that minimize $W_\lambda[g]$ thus represent a particular balance between statistical and systematic errors, as dictated by the λ parameter. For small λ the estimator $\rho_\epsilon^\lambda(E)$ is close to $\rho_\epsilon(E)$ but with a large statistical uncertainty. Conversely, for large λ the estimator $\rho_\epsilon^\lambda(E)$ has a small statistical error but differs significantly from $\rho_\epsilon(E)$.

When evaluated at the minimum, the functional $W_\lambda[g]$ is a function of λ only, thus defining $W(\lambda) \equiv W_\lambda[g^\lambda]$ at $g_\tau = g_\tau^\lambda$. The recipe suggested in Ref. [1] to choose the optimal value of the trade-off parameter determines $\lambda_\star$ such that

$$\left.\frac{\partial W(\lambda)}{\partial \lambda}\right|_{\lambda=\lambda_\star} = 0\;. \tag{19}$$

A straightforward application of Eq. (17) demonstrates that at $\lambda_\star$ (the maximum of $W(\lambda)$ where $g_\tau^\lambda = g_\tau^\star$) one has $A[g^\star] = A[0]B[g^\star]$. This can be understood as the condition of 'optimal balance' between statistical and systematic errors. The numerical results discussed in the following have been obtained using this recipe. In the rest of the paper, unless explicitly stated, we do not distinguish the theoretical quantity $\rho_\epsilon(E)$ from its numerical estimator $\rho_\epsilon^{\lambda_\star}(E)$. Estimates of the systematic error on $\rho_\epsilon(E)$ induced by the residual difference $\delta_\epsilon^{\lambda_\star}(E,\omega) - \delta_\epsilon(E,\omega)$ are discussed in Sec. V).

A defining feature of the approach in Ref. [1] is that the smearing function $\delta_\epsilon(E,\omega)$ and the associated values of ϵ and E are inputs of the algorithm, in contrast to the original Backus-Gilbert method [9, 10]. This work exploits this by employing four functional forms for the smearing kernel, each of which is a function of $x = E - \omega$:

$$\delta_\epsilon^{\mathsf{g}}(x) = \frac{1}{\sqrt{2\pi}\epsilon}\exp\left[-\frac{x^2}{2\epsilon^2}\right], \qquad \delta_\epsilon^{\mathsf{c0}}(x) = \frac{1}{\pi}\frac{\epsilon}{x^2+\epsilon^2}\,, \tag{20}$$

$$\delta_\epsilon^{\mathsf{c1}}(x) = \frac{2}{\pi}\frac{\epsilon^3}{(x^2+\epsilon^2)^2}\,, \qquad \delta_\epsilon^{\mathsf{c2}}(x) = \frac{8}{3\pi}\frac{\epsilon^5}{(x^2+\epsilon^2)^3}\,. \tag{21}$$

Here g and c stand for 'Gauss' and 'Cauchy' respectively, and the number following c gives the order of the Cauchy-like pole as shown. All kernels are normalized to unit area.

Given estimates of $\rho_\epsilon(E)$ over a range of ϵ for each of the resolution functions shown above, the final step in determining $\rho(E)$ is to perform an $\epsilon \to 0$ extrapolation. To this end it is useful to understand the small-ϵ expansion

[4] The parameter E_0 can be adjusted by exploiting the fact that $\rho(E)$ has support only for $E > 2m$, so that $\rho_\epsilon(E)$ in Eq. (11) is insensitive to the value of $\delta_\epsilon(E,\omega)$ for $\omega < 2m$. The same holds for $\rho_\epsilon^\lambda(E)$ so that the functional form of $\delta_\epsilon^\lambda(E,\omega)$ can be left unconstrained for $\omega < 2m$. It follows that any $E_0 \le 2m$ is a viable choice in determining the coefficients g_τ^λ. Therefore E_0 can be chosen to improve the numerical stability of the minimization procedure.

at fixed E. We consider these expansions only at energies away from singularities, i.e. away from $2m\mathbb{Z}^+$. At such points the smeared spectral function satisfies

$$\rho_\epsilon^{\mathsf{x}}(E) \equiv \int_0^\infty d\omega\, \delta_\epsilon^{\mathsf{x}}(E-\omega)\,\rho(\omega) = \rho(E) + \sum_{k=1}^{\infty} w_k^{\mathsf{x}} a_k(E)\epsilon^k\,, \tag{22}$$

where the superscript x labels a particular smearing kernel. As indicated in the final equality, the $O(\epsilon^k)$ contribution to the expansion can be decomposed into a geometric kernel-dependent coefficient w_k^{x} and a kernel-independent factor $a_k(E)$ which depends on $\rho(E)$. Tab. I summarizes the values of w_k^{x} for the four kernels used in this work. The ambiguity in separating w_k^{x} and $a_k(E)$ is fixed by setting $w_k^{\mathsf{c0}} = 1$ for all k. For this choice, all remaining w_k^{x} are simple rational numbers and

$$a_k(E) = \begin{cases} \frac{(-1)^{k/2}}{k!}\left(\frac{d}{dE}\right)^k \rho(E)\,, & k \text{ even} \\ \lim_{\eta\to 0^+} \frac{(-1)^{(k-1)/2}}{2\pi}\int_{-\infty}^{\infty} \mathrm{d}\omega\, \frac{\rho(E+\omega)+\rho(E-\omega)}{(\omega+i\eta)^{k+1}}\,, & k \text{ odd} \end{cases}\,. \tag{23}$$

III. FINITE-VOLUME ESTIMATOR

The theory is considered here on an $L \times T$ volume with periodic boundary conditions in both directions. Finite-L and finite-T effects on the spectral function are significantly different. On the one hand, finite-T (or thermal) effects are shown below to be exponentially suppressed and are therefore reliably small. On the other hand, the spectral function is dramatically different at finite and infinite L.

At infinite L the spectral density $\rho(E)$ defined in Eq. (7) is a continuous function which is analytic for all E except for $E = n\,m$ where n is a positive even integer. At finite L the spectrum of the Hamiltonian is discrete and the spectral function is a sum of Dirac δ-functions. As L increases, the spectrum of the Hamiltonian becomes denser and denser so that the continuous $L = \infty$ spectral density is recovered as a weak (or distributional) limit. In no meaningful way can this limit be considered point-wise and the finite-L effects on $\rho(E)$ treated as small corrections. Questions such as "Are the finite-L corrections to $\rho(E)$ exponentially suppressed?" are simply ill-posed. In contrast, smeared spectral functions converge to their infinite-L value in a point-wise sense. An immediate consequence of this discussion is that the $L \to \infty$ and $\epsilon \to 0^+$ limits (where ϵ is the width of the smearing kernel) do not commute and make sense only in a precise order: the $L \to \infty$ limit must be taken before the $\epsilon \to 0^+$ limit.

We know that individual finite-L matrix elements at energies above the two-particle threshold approach their infinite-L limit with corrections that vanish as inverse powers of $1/L$. When smeared spectral densities are considered, one may hope that finite-L corrections vanish faster than any inverse power in $1/L$, at least if the smearing function is 'reasonable enough'. This issue is explored in App. C, which considers a fictitious system where the infinite-L spectral density is given entirely by the 2-particle contribution in Eq. (9). The finite-L spectral density is then determined (up to exponential corrections) by the Lellouch-Lüscher formalism [14, 15]. One sees explicitly that the smeared spectral function has finite-L contributions which are $O(e^{-mL})$ in the case of the gaussian kernel, despite the power-law corrections to the individual energies and matrix elements. For the Cauchy kernels the effects are also exponentially suppressed by $O(e^{-\mu L})$ where $\mu \le m$ depends on the values of E, ϵ and m as

In the derivation of the exponentially-suppressed finite-L contributions, the analyticity of the smearing kernel plays a central role, and one can see that smooth but non-analytic kernels produce finite-L corrections that decay faster than any inverse power of L but generally not exponentially. We also observe that the asymptotic large-L regime is reached only after a fairly large intermediate oscillatory region. We do not claim that these findings are valid beyond the simple exercise considered here, but it is clear that the landscape of phenomena related to the $L \to \infty$ limit of smeared spectral functions is rich.

After this lengthy introduction, we give some explicit formulae. At finite L and T, the zero-momentum current-current correlator has the following Hamiltonian representation

$$C_{T,L}(t) = \frac{1}{L}\frac{\mathrm{tr}\left\{\mathrm{e}^{-(T-t)\hat{H}_L}\hat{A}\mathrm{e}^{-t\hat{H}_L}\hat{A}\right\}}{\mathrm{tr}\,\mathrm{e}^{-T\hat{H}_L}}\,, \tag{24}$$

where the definition

$$\hat{A} = \int_0^L d\boldsymbol{x}\,\hat{j}_1(\boldsymbol{x}) \tag{25}$$

is employed. At finite L the spectrum of the Hamiltonian is discrete. By introducing an orthonormal basis of energy eigenstates $|n\rangle_L$ satisfying $\hat{H}_L|n\rangle_L = E_n(L)|n\rangle_L$, one easily derives the spectral representation of the correlator

$$C_{T,L}(t) = \int_{-\infty}^{\infty} d\omega\, \tilde{\rho}_{T,L}(\omega) e^{-t\omega}\,, \tag{26}$$

with the definition

$$\tilde{\rho}_{T,L}(\omega) = \frac{1}{L}\sum_{n,n'} \frac{e^{-TE_{n'}(L)}}{\sum_{n''} e^{-TE_{n''}(L)}} \left|\langle n'|\hat{A}|n\rangle_L\right|^2 \delta(E_n(L) - E_{n'}(L) - \omega)\,. \tag{27}$$

Notice that $\tilde{\rho}_{T,L}(\omega)$ is non-vanishing also for negative values of ω. By separating terms with $E_n \geq E_{n'}$ and $E_n \leq E_{n'}$, and taking care to avoid double counting contributions with $E_n = E_{n'}$, one can split $\tilde{\rho}_{T,L}(\omega)$ into

$$\tilde{\rho}_{T,L}(\omega) = \rho_{T,L}(\omega) + e^{T\omega}\rho_{T,L}(-\omega)\ , \tag{28}$$

where the spectral density

$$\rho_{T,L}(E) = \frac{1}{L}\sum_{E_n \geq E_{n'}} \frac{e^{-TE_{n'}(L)}}{\sum_{n''} e^{-TE_{n''}(L)}} \left(1 - \frac{\delta_{E_n,E_{n'}}}{2}\right) \left|\langle n'|\hat{A}|n\rangle_L\right|^2 \delta(E_n(L) - E_{n'}(L) - E)\,, \tag{29}$$

vanishes for $E < 0$. By plugging this information in the correlator, we obtain the spectral representation in the form

$$C_{T,L}(t) = \int_{0^-}^{\infty} dE\, \rho_{T,L}(E)\{e^{-tE} + e^{-(T-t)E}\}\,. \tag{30}$$

As described in Sec. II, for a target smearing function $\delta_\epsilon(E-\omega)$, one now seeks an approximation $\delta_\epsilon^\lambda(E,\omega)$ in the space generated by the function basis

$$b_{T,\tau}(\omega) = e^{-a\tau\omega} + e^{-(T-a\tau)\omega} \tag{31}$$

by minimizing the functional $W_\lambda[g]$. Then

$$\rho^\lambda_{T,L,\epsilon}(E) = a\sum_{\tau=1}^{\tau_{\max}} g_\tau^\lambda C_{T,L}(a\tau) = \int_{0^-}^{\infty} dE\, \rho_{T,L}(E)\delta_\epsilon^\lambda(E,\omega) \tag{32}$$

is an approximation for the smeared spectral density

$$\rho_{T,L,\epsilon}(E) = \int_{0^-}^{\infty} dE\, \rho_{T,L}(E)\delta_\epsilon(E-\omega)\,. \tag{33}$$

A couple of comments on these formulae are in order. *(1)* The considered estimator (32) depends on $\tau_{\max}$, but (as demonstrated in Sec. V) our results are rather insensitive to its particular value. *(2)* The coefficients g_τ^λ obtained by solving the minimization problem in Eq. (17) depend on L and T via the covariance matrix appearing in $B[g]$, and on T via our choice of the basis $b_{T,\tau}(\omega)$. In the limit of infinite statistics (with $B[g] = 0$), the g_τ^λ depend on T but not on L.

Eq. (29) makes manifest that finite-temperature effects on the spectral density at fixed L are exponentially suppressed, i.e.

$$\rho_{T,L}(E) = \rho_{\infty,L}(E) + O(e^{-Tm(L)}) = \frac{1}{L}\sum_n \left|\langle 0|\hat{A}|n\rangle_L\right|^2 \delta(E_n(L) - E) + O(e^{-Tm(L)})\,, \tag{34}$$

where $m(L)$ is the energy gap in finite volume. Smearing the spectral function amounts to replacing the Dirac δ-function in Eq. (29) with the smearing kernel δ_ϵ. At fixed L the smeared spectral density also has finite-temperature effects that are exponentially suppressed with $O(e^{-Tm(L)})$. Even though far from obvious, it is reasonable to assume that finite-T effects are exponentially suppressed also at $L = \infty$ since the theory has a mass gap.

ID	$(L/a)\times(T/a)$	β	$am_\star$	$m_\star L$	$m_\star T$	$N_{\rm th}\times 10^{-6}$	$N_{\rm rep}$	$N_{\rm bin}$	$B\times 10^{-6}$	$N_{\rm c}\times 10^{-10}$
A1	640×320	1.63	0.0447989(62)	29	14	1.6	480	5	3.2	3.84
A2	1280×640	1.72	0.0257695(31)	33	17	12.8	3840	1	20	7.6
A3	1920×960	1.78	0.0176104(31)	34	17	12.8	7680	1	10	7.6
A4	2880×1440	1.85	0.0112608(29)	32	16	12.8	30720	1	2.5	7.68
B1	5760×1440	1.85	0.0112607(73)	65	16	12.8	7680	1	1.5	1.152
B2	2880×2880	1.85	0.0112462(72)	32	32	12.8	7680	1	1.5	1.152

TABLE II. Details for the ensembles of field configurations generated for this work. The dimensionful scale $m_\star \simeq m$ is defined in Eq. (39). Ensembles A1-A4 enable the continuum limit at approximately fixed physical volume, while B1 and B2 are used to estimate finite size effects. Each ensemble consists of $N_{\rm rep}$ independent identical replica, each of which is thermalized for $N_{\rm th}$ cluster updates before $N_{\rm bin}$ measurements are taken by averaging over B subsequent updates. This results in a total number of measurement cluster updates $N_{\rm c}$ for ensemble. Only two digits are given for $m_\star L$ and $m_\star T$.

IV. LATTICE-DISCRETIZED MODEL

We calculate the Euclidean current-current correlator in Eq. (30) by numerical simulation of the lattice-discretized model. The field $\sigma(x)$ is now defined on the set of $(L/a)\times(T/a)$ equally-spaced points $x=(a\tau,\boldsymbol{x})$ on the two-torus, denoted by Λ. The standard discretization of the action is employed here

$$S[\sigma]=\frac{\beta}{2}\sum_{x\in\Lambda}a^2\sum_\mu\hat\partial_\mu\sigma(x)\cdot\hat\partial_\mu\sigma(x)=\beta\sum_{x\in\Lambda}\sum_\mu\left[1-\sigma(x)\cdot\sigma(x+a\hat\mu)\right]\,, \tag{35}$$

where $\hat\partial_\mu f(x)=\frac{1}{a}[f(x+a\hat\mu)-f(x)]$ is the forward-difference operator defined with periodic boundary conditions in both directions. Expectation values of observables are given by the path integral

$$\langle A\rangle=\frac{1}{Z}\int\left[\prod_{x\in\Lambda}\mathrm{d}\sigma(x)\right]\,\mathrm{e}^{-S[\sigma]}A[\sigma]\,, \tag{36}$$

where $\mathrm{d}\sigma(x)$ denotes the O(3)-invariant integration measure over the unit sphere. The global O(3) symmetry is preserved by the lattice discretization, and its associated Noether current is

$$j^a_\mu(x)=\beta\epsilon^{abc}\sigma^b(x)\hat\partial_\mu\sigma^c(x)\,. \tag{37}$$

Exact O(3) Ward identities imply that this current is renormalized. The discretized version of the zero-momentum Euclidean current-current correlator is given by

$$C(a\tau)=\sum_{\boldsymbol{x}}a\langle j^a_1(x)\,j^a_1(0)\rangle\,. \tag{38}$$

The strong dynamics of the O(3) model generate a mass gap m, which is often used to set the scale. In this work we choose to measure all dimensionful quantities in units of the appropriate power of the mass scale $m_\star$, defined by the equation [16]

$$m_\star^{-1}C(m_\star^{-1})=0.046615\,. \tag{39}$$

While in principle one can choose any number in the right-hand side, we use a value that gives $m_\star\simeq m$. In fact, by using the correlator reconstructed from the 2-, 4- and 6-particle contributions to the spectral function we find that the relative difference between m and $m_\star$ is of order 10^{-5}. In practice the correlator $C(t)$ is known only at values of $t=a\tau$ that are integer multiples of the lattice spacing a, and the equation for $m_\star$ is solved using a piecewise linear interpolation of $\log tC(t)$. The quantity $m_\star$ is determined with higher statistical precision than m and is also affected by smaller finite-volume effects.

Numerical simulations are performed with the single-cluster algorithm described in App. D. Details concerning the generated ensembles of field configurations are summarized in Tab. II. The ensembles A1, A2, A3, A4 have different values of β and therefore different values of the lattice spacing, but similar $m_\star L\geq 29$ and $m_\star T\geq 14$. The ensembles B1 and B2 have been generated with the same lattice spacing as A4 but with doubled spatial and temporal extent, respectively. While the ensembles A1, A2, A3, and A4 are used to perform a continuum extrapolation, B1 and B2 enable estimates of the residual finite-L and finite-T effects, as explained in Sec. V.

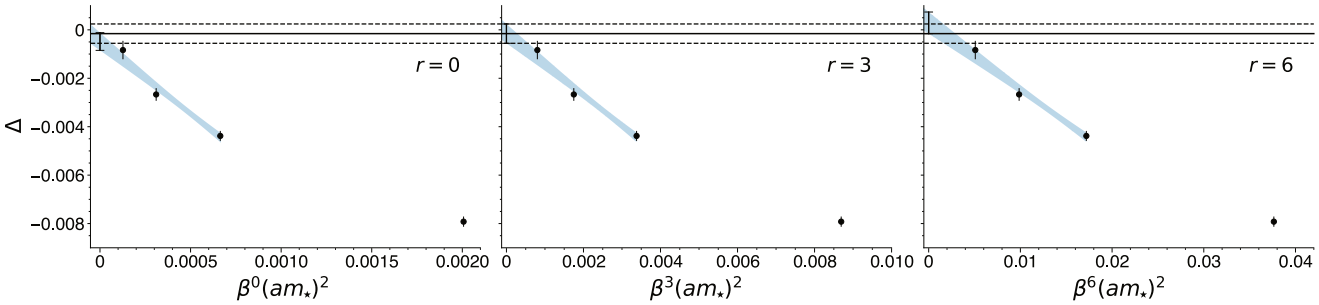

FIG. 1. Illustration of the continuum limit procedure for $tC(t)|_{m_\star t=0.5}$. Three different extrapolation forms are employed using Eq. (41) with $r = 0, 3, 6$. Shown is the difference between the numerical estimate and the exact result divided by the exact result, denoted Δ. The horizontal band indicates our estimate for the continuum extrapolated Δ, given by the intercept from the fit with $r = 3$. The statistical error on this estimate is similar to the variation across the three values of r, which are taken as an estimate of the systematic error. This validates the use of the 'phenomenological' extrapolation forms in Eq. (41) for $\rho_\epsilon(E)$ where the statistical errors are larger.

The standard discretization of the 2-dimensional O(3) σ-model employed here is known to approach the continuum limit rather slowly. Ref. [17] observed that lattice artifacts behave like $O(a)$ over a large range of lattice spacings, in apparent contradiction with Symanzik's effective theory, which predicts an asymptotic $O(a^2)$ behavior up to logarithms. The puzzle was solved in [18, 19]: the asymptotic behavior is correctly described by Symanzik's effective theory, but the logarithmic corrections turn out to be large and must be included in fitting formulae used to extrapolate to the continuum limit. On-shell quantities, such as the mass gap or energy levels in finite volume, have the asymptotic expansion

$$Q(a) = Q(0) + Ca^2\beta^3 \left[1 + \sum_{k=1}^{\infty} c_k \beta^{-k}\right] + O(a^4)\,, \tag{40}$$

where c_1 and c_2 are universal and calculable in terms of two-loop and three-loop integrals respectively ($c_1 = -1.1386\ldots$ is analytically known and $c_2 = -0.4881$ is estimated numerically in Ref. [19]), while the other constants are non-perturbative. The leading logarithm β^3 is generated by the dimension-four operator with largest one-loop anomalous dimension appearing in the Symanzik expansion of the action. The current two-point function, and consequently its spectral function, get extra contributions from dimension-three operators appearing in the Symanzik expansion of the current. These one-loop anomalous dimensions are unknown, and their calculation is well beyond the scope of this work. For the continuum extrapolation of the smeared spectral functions we use a fit function of the type

$$Q(a) = Q(0) + Ca^2\beta^r\,, \tag{41}$$

where the exponent r is fixed to $0, 3, 6$, and $Q(0)$ and C are fit parameters. We take $Q(0)$ at $r = 3$ as our continuum extrapolation and the spread generated by the three values of r as an estimate of the systematic error. One may argue that, since a β^3 term exists in the Symanzik expansion, the correct asymptotic formula should have $r \geq 3$. However it is conceivable that the coefficients of the various logarithms may conspire in such a way that an effective power $r < 3$ is generated in some intermediate regime. We therefore choose to include also $r = 0$ in our analysis. As is evident in Fig 1, the variation of r across 0, 3, and 6 has little effect on the continuum extrapolation of $tC(t)$ with $t = 0.5m_\star^{-1}$ using our three finest lattice spacings. These conclusions are supported by additional extrapolations at several values of t in the range $t \in [0.5m_\star, 4m_\star]$. This strategy is thus adopted in Sec. V for continuum extrapolations of $\rho_\epsilon(E)$, where the fourth lattice spacing is included for stability in the presence of larger statistical errors on $\rho_\epsilon(E)$.

V. NUMERICAL RESULTS

After detailing investigations into the systematic errors, this section presents the numerical verification of the spectral reconstruction procedure using two different tests. The first test (discussed in Sec. V A) compares $\rho_\epsilon(E)$ with exact results at fixed smearing width ϵ for each of the four smearing kernels in Eq. (20). As anticipated, $\rho_\epsilon(E)$ is more difficult to determine with increasing E and decreasing ϵ. The second test, which is detailed in Sec. V B, uses $\rho_\epsilon(E)$ at finite ϵ to extrapolate to the $\epsilon \to 0$ limit and obtain the unsmeared spectral function $\rho(E)$. The extrapolation procedure (as applied here) requires smearing widths that are small compared to the scale at which the unsmeared

spectral function varies, and is therefore less effective in the elastic region where $\rho(E)$ increases rapidly with the onset of two-particle phase space. Since $\rho(E)$ in the elastic region is accessible to the finite-volume formalism, the focus is instead on energies in the inelastic region $E > 4m$. Due to the absence of any sharp 'resonance peaks', $\rho(E)$ varies increasing slowly with increasing E, suggesting that the smearing width should be scaled $\epsilon \propto (E - 2m)$, i.e. with the distance to the rapid variation from the two-particle threshold. Apart from this scaling in the smearing width, the analysis for these two tests proceeds identically.

All statistical errors on the results presented here are estimated using the bootstrap procedure with $N_{\text{boot}} = 800$ bootstrap samples, generated independently on each ensemble from the $N_{\text{rep}} \times N_{\text{bin}}$ measurements listed in Tab. II. For all the reconstructions, the lower bound of the integration range E_0 defined in Eq. (16) is set using the scale $m_\star$ via $aE_0 = 2\,am_\star$ to (approximately) coincide with the two-particle threshold. This choice minimizes the range in energy over which the functional $A[g]$ forces the reconstructed and target kernels to be similar. The values of $am_\star$ given in Tab. II are also used to fix the dimensionful parameters ϵ and E at different lattice spacings. Properly including the statistical error on $am_\star$ requires the determination of the coefficients g_τ^λ on each bootstrap sample, which significantly increases the computational cost. After confirming that this has no observable effect on a selection of sample reconstructions, the statistical error on the values of $am_\star$ in Tab. II is subsequently ignored.

A. Fixed smearing width

Before presenting the main results of this section in Fig. 6, the systematic errors must be estimated. Consider first systematic errors due to the reconstruction procedure. Due to the finite number of input values $C(a\tau)$, the reconstructed smearing kernel will never be exactly equal to the desired one. This source of systematic error is quantified by the functional $A[g^\lambda]/A[0]$, defined in Eq. (16) as the (squared) two-norm of the difference normalized by the (squared) two-norm of the desired kernel. While this measure does not take into account the role of the unsmeared spectral function $\rho(E)$ on the systematic error of $\rho_\epsilon(E)$, this error certainly vanishes in the $A[g^\lambda] \to 0$ limit. The value of $A[g^\lambda]$ is therefore a useful diagnostic for determining the onset of the statistics-limited regime: if λ is lowered such that $A[g^\lambda]$ changes significantly and no significant change is observed in $\rho_\epsilon^\lambda(E)$, then this source of systematic error is likely smaller than the statistical error. This type of 'plateau' analysis is well-known to lattice field theory practitioners and is exemplified in Fig. 2. As discussed in Sec. II, we follow here the recipe of Ref. [1] and quote as the central value for $\rho_\epsilon(E)$ the result obtained at $\lambda = \lambda_\star$, defined in Eq. (19).

Another probe of the systematic error due to the reconstruction is the comparison of $\rho_\epsilon(E)$ determined from coefficients subject to various constraints on the minimization, implemented via Lagrange multipliers as explained in App. B. Fig. 2 shows results for the unconstrained reconstruction, the constraint that the reconstructed smearing kernel has a signed area equal to the desired one, and the constraint that the reconstructed kernel exactly coincides with the desired one at the peak $\omega = E$. For large λ, these different reconstructions differ significantly[5] but coincide well within the statistical error at $\lambda_\star$, lending additional confidence that $\lambda_\star$ is indeed in the statistics-dominated regime. Put more precisely, reconstructions subject to different constraints result in different reconstructed smearing kernels. Their consistency when compared at similar values of $A[g^\lambda]/A[0]$ demonstrates that these differences are insignificant and suggests that deviations from the exact kernel are as well. Overall, the approach employed for choosing $\lambda_\star$ discussed in Eq. (19) to balance statistical and systematic errors is somewhat conservative. Fig 2 suggests the less restrictive alternative strategy of demanding consistency between the three different reconstructions. This could potentially result in smaller statistical errors, but requires further investigation beyond the scope of this work.

In addition to this, the sensitivity to the input correlator data is probed in Fig. 3. The input correlator time slices $\{C(a\tau)\}$ range over $[\tau_{\min}, \tau_{\max}]$ with $\tau_{\min} = 1$ fixed. The input time slices are correlated and suffer from an exponential degradation of the signal-to-noise ratio with increasing τ with a rate phenomenologically similar to m. As shown in Fig. 3 for a sample reconstruction, $\rho_\epsilon(E)$ is relatively insensitive to $\tau_{\max}$, and to a 'thinning' of the input data, so that the time slices are separated by $\sigma_t = a(\tau_{n+1} - \tau_n)$. These observations can be plausibly explained by the signal-to-noise degradation and correlation of the input data. The role of $B[g]$ is to penalize coefficients g_τ^λ which would result in a large statistical error. This penalty naturally disfavors input data at large τ, effectively 'turning off' these time slices and resulting in an insensitivity to $\tau_{\max}$. Similarly, the correlation between the input time slices may be responsible for the robustness to changing σ_t. Both of these hypotheses require further study beyond the scope of the present work.

After demonstrating that the reconstruction procedure on a particular ensemble of field configurations results in a statistics-dominated estimator for $\rho_\epsilon(E)$, we turn now to systematic errors associated with the finite extent of the

[5] The equal area constraint is somewhat weaker than demanding $\delta_\epsilon^\lambda(E,\omega) = \delta_\epsilon^\kappa(E-\omega)$ at $\omega = E$, as evidenced by the plots of $\delta_\epsilon^\lambda(E,\omega)$ in the center and left panels of Fig. 2.

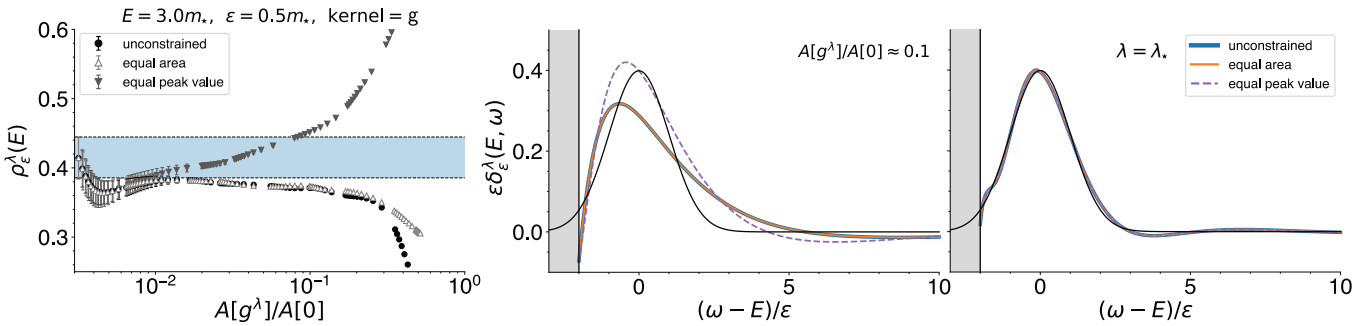

FIG. 2. For the A1 ensemble detailed in Tab. II, an illustration of the compromise between statistical and systematic errors which results from choosing $\lambda = \lambda_\star$. **Left**: the estimator $\rho_\epsilon^\lambda(E)$ for the smeared spectral function at different values of λ, plotted against the 'resolution' functional $A[g^\lambda]/A[0]$ defined in Eq. (16). The horizontal band indicates the result at $\lambda_\star$ (where $A[g^\star] = A[0]B[g^\star]$) without any constraints on the determination of the optimal coefficients. This choice is consistent with the one obtained by imposing the equal area constraint (denoted 'equal area') as well as with the one demanding that reconstructed smearing kernel take the correct value at the peak, denoted 'equal peak value'. **Center**: the reconstructed smearing kernel $\delta_\epsilon^\lambda(E,\omega)$ for the different constraints together with the target kernel $\delta_\epsilon^{\mathrm{g}}(E-\omega)$ shown as a solid line. The value of λ for each of the three reconstructions results in $A[g^\lambda/A[0] \approx 0.1$. **Right**: same as the center panel but with $\lambda = \lambda_\star$.

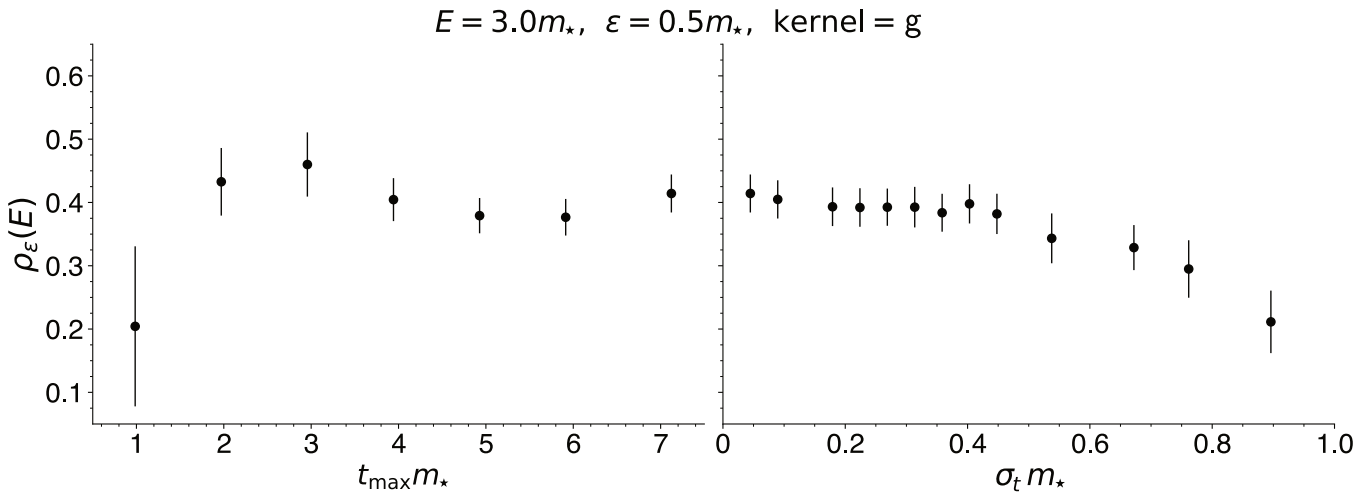

FIG. 3. **Left**: test of the sensitivity of the reconstruction procedure to the range of time slices $[\tau_{\mathrm{min}}, \tau_{\mathrm{max}}]$ by varying τ_{max}, plotted using $t_{\mathrm{max}}m_\star = \tau_{\mathrm{max}}(am_\star)$ with fixed $\tau_{\mathrm{min}} = 1$. **Right**: test of the sensitivity to the spacing between time slices included in the reconstruction σ_t. Both tests are performed on the A1 ensemble detailed in Tab. II. Evidently the reconstruction procedure is relatively stable under the variation of σ_t and τ_{max}.

lattice. Along the (approximate) line of constant physics defined by the ensembles A1-A4, these errors are crudely estimated by considering separately the differences between B1 and A4, and B2 and A4. These differences

$$\Delta_{\mathrm{L}}(\epsilon, E) = \rho_\epsilon^{L,T}(E) - \rho_\epsilon^{2L,T}(E) \qquad \text{and} \qquad \Delta_{\mathrm{T}}(\epsilon, E) = \rho_\epsilon^{L,T}(E) - \rho_\epsilon^{L,2T}(E) \tag{42}$$

are taken as estimators for the systematic errors due to the finite L and T and are added (in absolute value) independently for each ϵ, E, and smearing kernel. A selection of these deviations are shown in Fig. 4, illustrating that they are at most marginally significant. Nonetheless, this systematic error is subsequently taken into account and represents the largest of the systematic error estimates. Although Eq. (34) ensures that finite-T effects are 'reliably' $\mathrm{O}(\mathrm{e}^{-mT})$, we conservatively account for both finite L and T with additional systematic errors. An increase of statistics on the B1 and B2 ensembles would more accurately estimate these systematic errors and provide a more stringent test of the error estimates due to the reconstruction, but is left for future work.

In addition to finite size effects, systematic errors due to the lattice spacing must be estimated as outlined in Sec. IV. The continuum limit is taken with four lattice spacings using the ensembles A1-A4, but (as detailed in Sec. IV) the asymptotic a^2 behavior is affected by large logarithmic corrections and the 'phenomenological' extrapolation form of Eq. (41) is employed with $r = 0$,3, and 6. The value at $r = 3$ is taken as the best estimate and the largest deviation

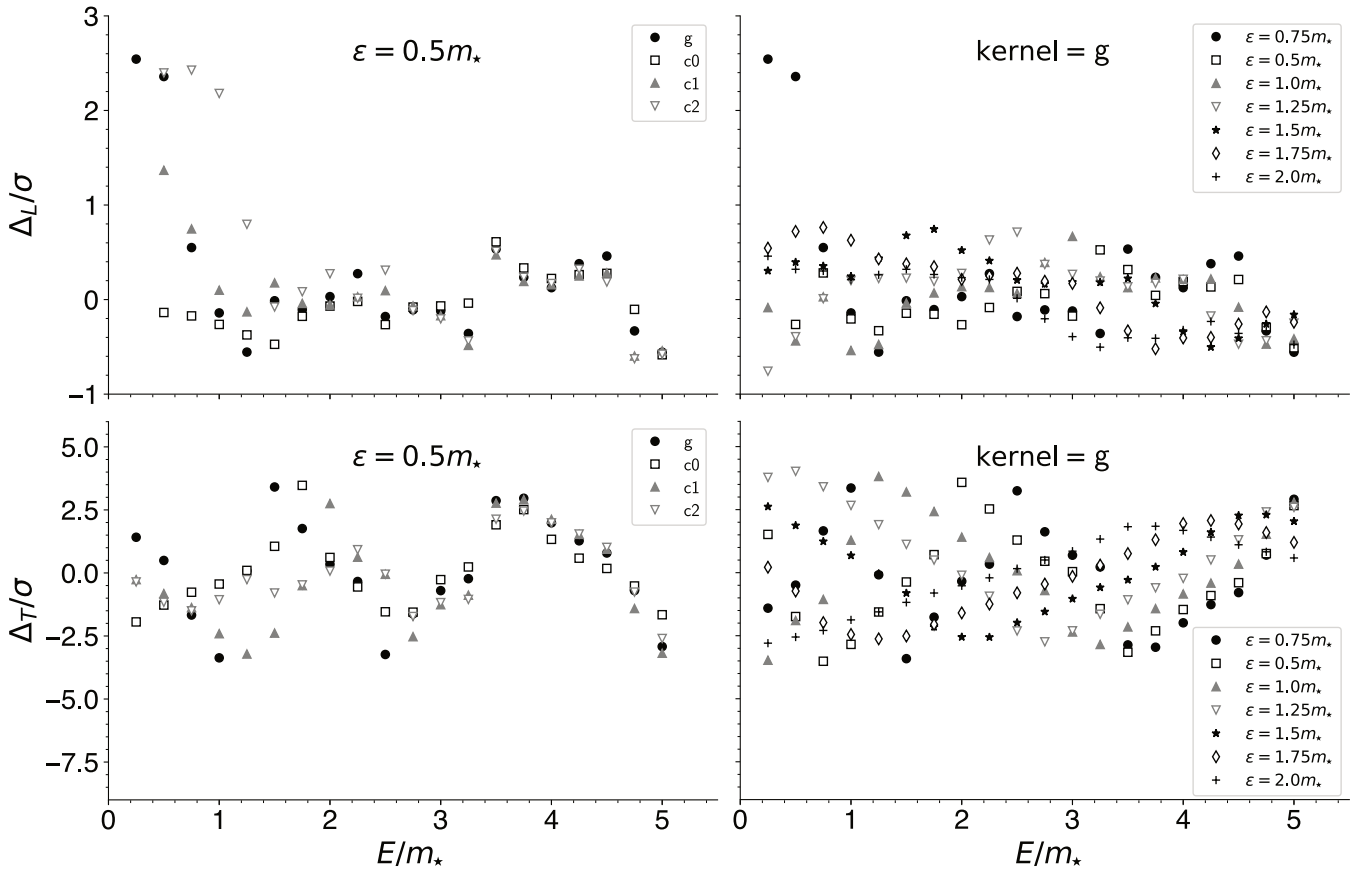

FIG. 4. The differences $\Delta_{\mathrm{L}} = \rho_\epsilon^{2L,T} - \rho_\epsilon^{L,T}$ and $\Delta_{\mathrm{T}} = \rho_\epsilon^{L,2T} - \rho_\epsilon^{L,T}$ from Eq. (42). The vertical axis is normalized by the error on the estimated difference and can be interpreted as the statistical significance of each of the finite size effects. The sum of the mean values $|\Delta_{\mathrm{L}}| + |\Delta_{\mathrm{T}}|$ is taken as an estimate of the systematic error due to finite size effects independently for each E, ϵ, and smearing kernel.

between any two as an estimate of the systematic error. A selection of the extrapolations for the three different values of r is shown in Fig. 5. Evidently, the difference in the extrapolated value varies little across these three extrapolation forms.

After estimating systematic errors due to the reconstruction, finite lattice size, and finite lattice spacing, the results for $\rho_\epsilon(E)$ are at last confronted with the exact values. While no further systematic error is assigned to the reconstruction procedure, estimates of the remaining three sources of systematic error (finite L, finite T, continuum limit) are added naively. The total systematic error is then combined in quadrature with the statistical error on the continuum limit estimator. The finite-L and T errors are typically the dominant source of systematic error, and are typically similar in magnitude to the statistical error. A selection of these continuum extrapolated values are shown in Figs. 6. In the left two panels all four kernels are compared at a large fixed $\epsilon = 2m_\star$ to accentuate the difference between them. However, all of these results are consistent with the exact values (including 2-, 4-, and 6-particle contributions) within the combined statistical and systematic errors. The right two panels show various ϵ for the gaussian kernel are similarly consistent with the exact numbers. The increasing difficulty of the reconstruction problem with increasing E and decreasing ϵ is apparent.

B. Extrapolation to zero smearing width

The continuum extrapolated results for $\rho_\epsilon(E)$ displayed in Fig. 6 demonstrate that the spectral reconstruction procedure yields quantitatively accurate results within the quoted statistical and systematic errors. However, the difficulty in reconstructing $\rho_\epsilon(E)$ at large E and small ϵ naively suggests that the approach is of little use in the inelastic region, precisely where the finite-volume formalism is not yet developed. However, the increasing smoothness of $\rho(E)$ with increasing E can be exploited by scaling $\epsilon \propto (E - 2m_\star)$ in order to probe larger energies. The scaled

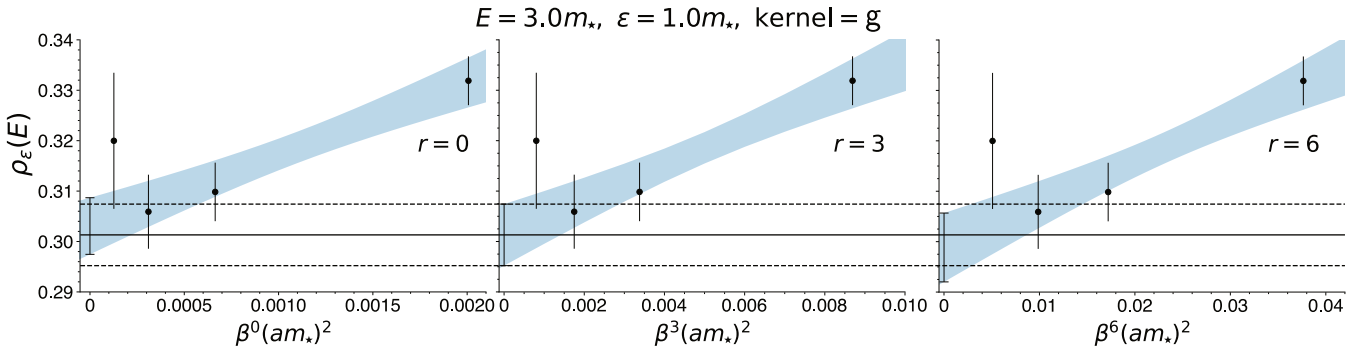

FIG. 5. Illustration of the continuum extrapolation procedure from Eq. (41) with $r = 0$, 3, and 6 at $E = 3m_\star$, $\epsilon = m_\star$, and the gaussian smearing kernel. The three panels show the $r = 0$ ansatz (left), the $r = 3$ (center), and the $r = 6$ (right). The black points are the continuum extrapolated value and horizontal band is the extrapolated value from $\beta^3 a^2$, which is taken as the best estimate. As in Fig. 1, there is evidently little variation across the different extrapolation forms.

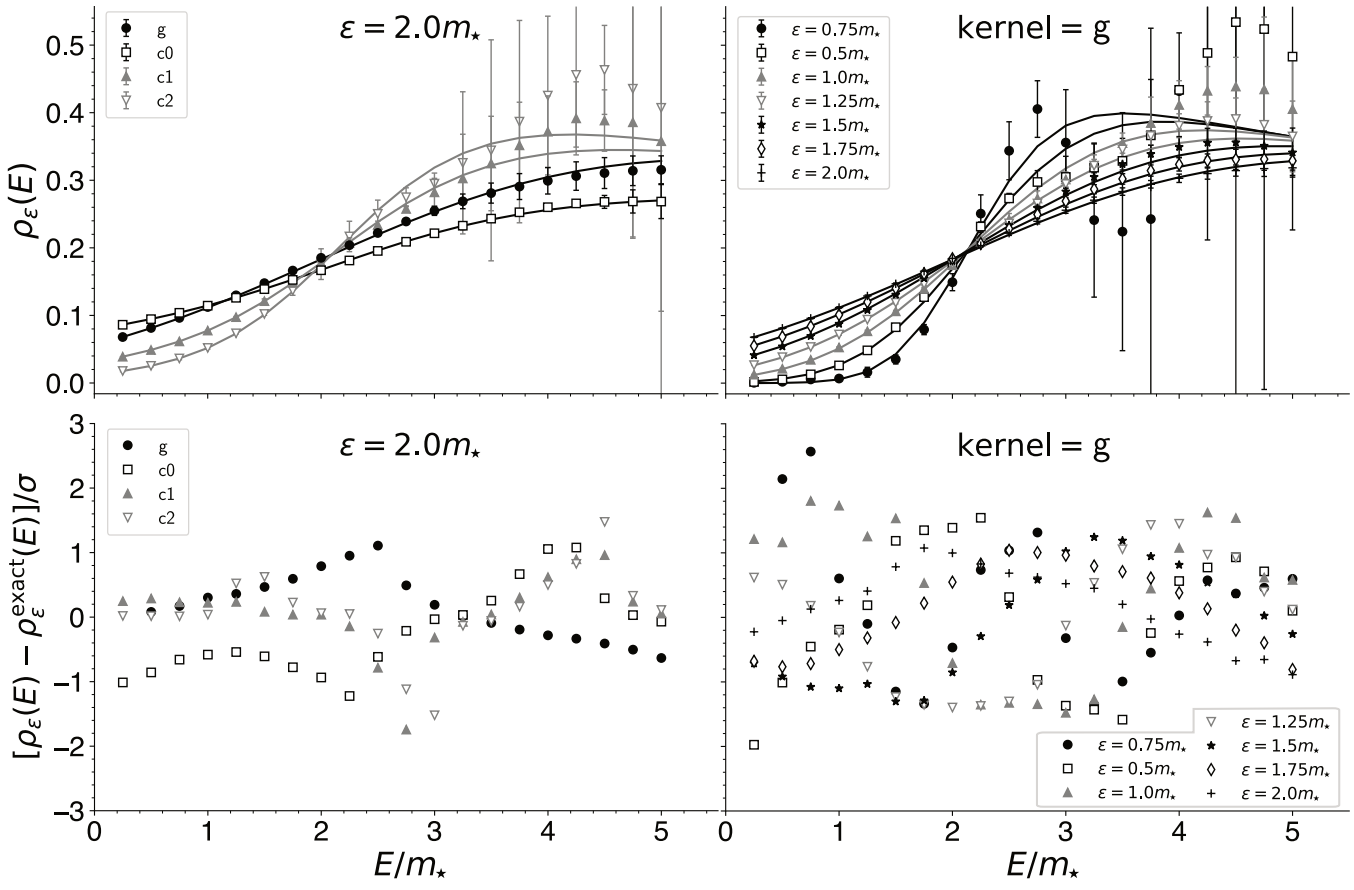

FIG. 6. Summary of the continuum extrapolated values with statistical and systematic errors combined in quadrature as described in the text. **Top left**: all four smearing kernels are plotted for a large smearing radius $\epsilon = 2m_\star$ together with the exact results including 2-, 4-, and 6-particle contributions shown as solid lines. **Bottom left**: the 'pull' between the numerical and exact results for the same data. The variation of the points indicates that the numerical and exact results are consistent at the 2-σ level. **Top and bottom right:** same type of plots but for a variety of smearing widths with the gaussian smearing kernel.

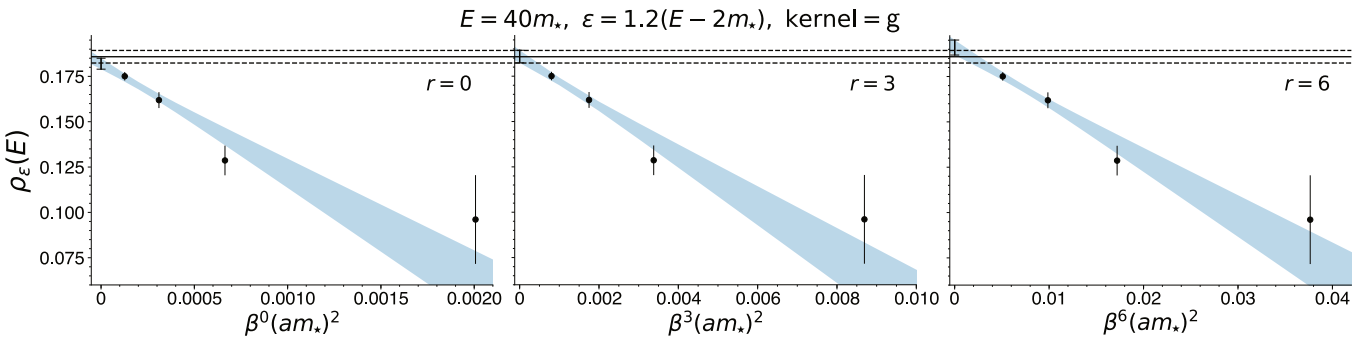

FIG. 7. The same as Fig. 5 for $E = 40m_\star$, $\epsilon = 1.2(E - 2m_\star)$, and the gaussian smearing kernel.

values of $\rho_\epsilon(E)$ are used to extrapolate $\epsilon \to 0$ and determine the unsmeared spectral function $\rho(E)$ using the small-ϵ expansion discussed in Sec. II. The rapid variation of $\rho(E)$ in the elastic region inhibits the application of this approach there, so we focus on $E \geq 4m_\star$[6]. The elastic region is also accessible to finite-volume methods, while no finite formalism currently exists to directly determine $n \geq 4$ particle contributions.

A natural concern is the growth of cutoff effects with increasing E and ϵ, since $\rho_\epsilon(E)$ has increasingly significant contributions from more energetic states. Fig. 7 shows the continuum extrapolations of $\rho_\epsilon(E)$ at the largest energy considered here, which is $E = 40m$, and $\epsilon = 1.2(E - 2m_\star)$, which is the largest ϵ used in the $\epsilon \to 0$ extrapolation. Although the continuum limit is somewhat steeper than those in Fig. 5, there is still little variation across the different values of r. However, it appears that the statistical error on the estimator $\rho_\epsilon^\lambda(E)$ decreases more rapidly with $am_\star$ in Fig. 7 than in Fig. 5. This phenomenon requires further study, but could be influenced by our choice of basis vectors, namely the inclusion of all $\tau \in [1, 160]$ at each lattice spacing. The edge of the Brillouin zone may also play a role since $1/am_\star \sim E/m_\star$ when $E \gtrsim 20m_\star - 90m_\star$.

The small-ϵ behavior of $\rho_\epsilon(E)$ depends on the smearing kernel[7]. As discussed in Sec. II, for the four smearing kernels considered here this dependence is encoded in the coefficients w_k^x, which are known analytically and given in Tab. I. The coefficients $a_k(E)$ in Eq. (22) however depend on $\rho(E)$ only and are therefore identical across the different smearing kernels. This means that an extrapolation ansatz which includes terms up to $O(\epsilon^n)$ contains $n+1$ fit parameters for each of the a_k, which are constrained by data from all the smearing kernels. In this work we target $a_0(E) = \rho(E)$ only: no additional information from the other $a_k(E)$ is used to further constrain $\rho(E)$.

The clear sources of systematic error in this approach are the extrapolation form and the extrapolation range $[\epsilon_{\min}, \epsilon_{\max}]$. Due to the difficulty in reconstructing small ϵ, the statistical errors increase with decreasing ϵ so that in practice varying $\epsilon_{\min}$ has little effect on the extrapolated value. We therefore fix $\epsilon_{\min} = 0.3(E - 2m_\star)$ for all smearing kernels and extrapolations. The effect of varying $\epsilon_{\max}$ must be monitored more closely, however. In order to fairly include data from different smearing kernels, $\epsilon_{\max}$ for each kernel is re-scaled $\epsilon_{\max} \to \epsilon_{\max}/\alpha_\mathsf{x}$ with $\int_{-\alpha_\mathsf{x}}^{\alpha_\mathsf{x}} \mathrm{d}x\, \delta_{\epsilon=1}^\mathsf{x}(x) = \mathrm{erf}(2^{-1/2}) \approx 0.68269$ chosen to approximately coincide with the gaussian. This treats the data from different smearing kernels on equal footing: all smearing widths are included up to those with the same amount of 'leakage' down to the two-particle threshold, where $\rho(E)$ varies rapidly. For the c0 kernel the large value $\alpha_{\mathsf{c0}} \approx 1.84$ together with the leading $O(\epsilon)$ behavior effectively renders it useless in the extrapolations. For the gaussian kernel $\alpha_\mathsf{g} = 1$ by definition, while $\alpha_{\mathsf{c1}} = 0.7$ and $\alpha_{\mathsf{c2}} = 0.855$ increase the fit range for these two kernels relative to the gaussian. The extrapolations are therefore performed with the three kernels g, c1, and c2. An example of such an extrapolation is shown in the left panel of Fig. 8.

The systematic error estimate due to the $\epsilon \to 0$ extrapolation proceeds by employing extrapolation forms up to and including $O(\epsilon^p)$ with $p = 2$, 3, and 4 and varying $\epsilon_{\max}$ keeping below $\epsilon_{\max} < 1.3(E - 2m_\star)$. For each value of p, the largest $\epsilon_{\max}$ resulting in a (correlated) χ^2/d.o.f. < 1 is identified, with the $p = 4$ value taken as the best estimate for $\rho(E)$. The spread of these three values is then added in quadrature as a systematic error. An example plot showing the consistency between different extrapolation forms and extrapolation ranges is shown in the right panel of Fig. 8. This procedure is performed for all energies for which $E/m_\star$ takes integral values from 4 to 40. A summary of the extrapolated results is shown in Fig. 9, which are consistent with the exact results including 2, 4, and 6 particle contributions. Interestingly, the data exhibits some sensitivity to $\rho^{(4)}(E)$ for $E \gtrsim 20m$. Four-particle

[6] The opening of subsequent $2n$-particle thresholds introduces non-analyticities in $\rho(E)$, but for the range of energies considered here $\rho(E)$ is dominated by fewer-particle contributions and therefore approximately smooth.

[7] For a fair comparison of the effectiveness of the four kernels in Eq. (20), ϵ for the c2 is enlarged by the rescaling $\epsilon \to \sqrt{3}\epsilon$ so that $w_2^{\mathsf{c2}} = 1$ in Tab. I. This rescaling is not employed for the c2 data in Sec. V A

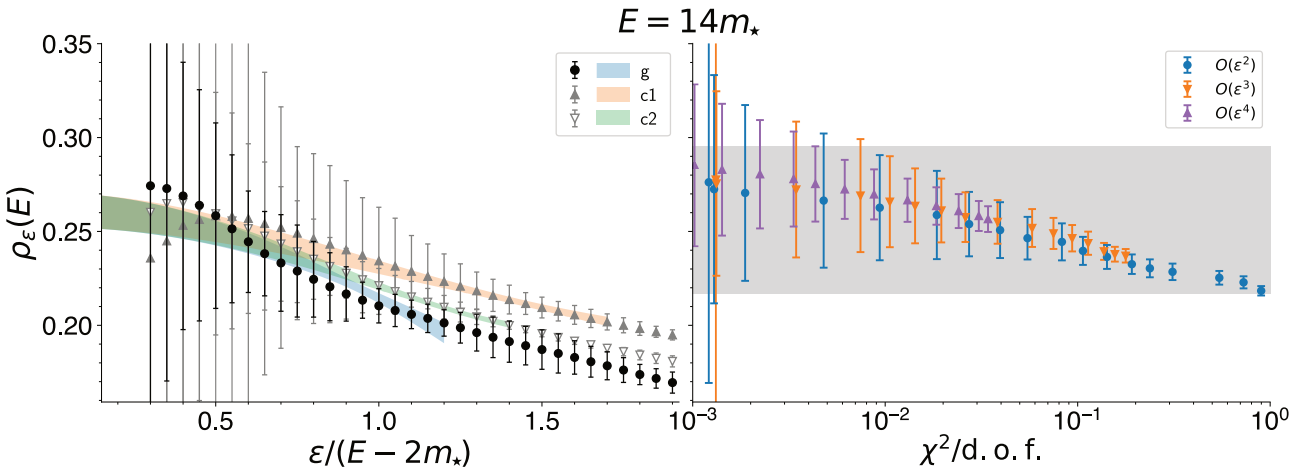

FIG. 8. **Left**: a sample constrained extrapolation of the g, c1, and c2 kernels at $E = 14m_\star$ with the (constrained) extrapolation form including terms up to $O(\epsilon^4)$. **Right**: summary of the extrapolated values for different extrapolations forms and different extrapolation ranges $[\epsilon_{\min}, \epsilon_{\max}]$ with $\epsilon_{\min} = 0.3(E - 2m_\star)$ fixed and varying $\epsilon_{\max}$. For each $\epsilon_{\max}$, the extrapolated result is plotted with the correlated χ^2/d.o.f. as the horizontal coordinate. The horizontal band shows the final estimate for the extrapolated values, with statistical and systematic errors combined in quadrature. The systematic errors are estimated as discussed in the text.

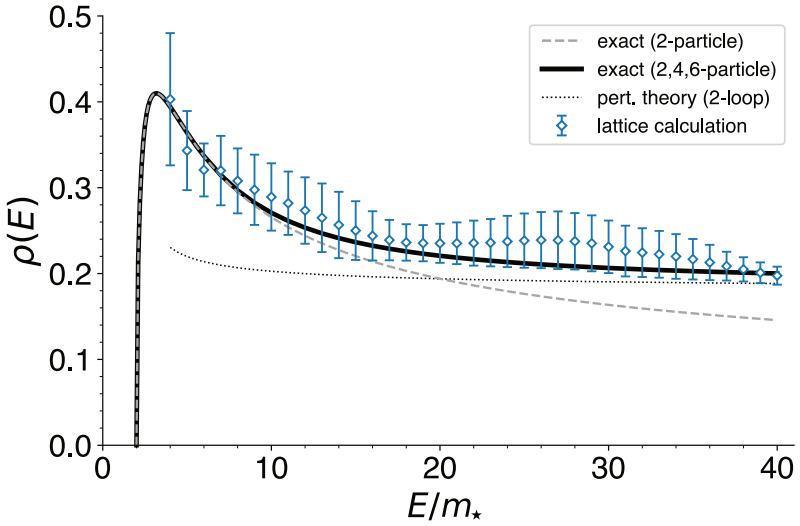

FIG. 9. A summary of the $\epsilon \to 0$ extrapolated results, together with the exact values two-particle contribution (light solid line) and the two-, four-, and six-particle contributions (dark solid line).

scattering amplitudes are currently beyond the reach of the finite-volume formalism.

VI. CONCLUSIONS

The aim of the preceeding sections is to verify the procedure for numerically computing smeared spectral functions (with an *a priori* specified smearing kernel) from lattice field theory correlation functions. In this regard the two-dimensional O(3) model usefully provides exact results against which the estimates can be checked. These checks, which are presented in Figs. 6 and 9, are satisfied and compare both $\rho_\epsilon(E)$ at finite ϵ and the results from extrapolations $\epsilon \to 0$ to determine $\rho(E)$ deep into the inelastic region where finite-volume methods have not yet been developed. The highest energy considered here is $E = 40m_\star$, at which $\rho(E)$ is determined with a relative accuracy of 5% and differs significantly from the exact two-particle contribution $\rho^{(2)}(E)$ given in Eq. (9).

Apart from the 'usual' sources of systematic error due to the finite lattice spacing and extents, we must also consider the imperfect reconstruction of the smearing kernel due to the finite number of input time slices and thier associated statistical errors. All sources of systematic error have been estimated and included in Figs. 6 and 9 where the statistical and systematic errors are added in quadrature. Generally the errors due to the finite lattice extent are largest, and are typically less than or comparable to the statistical errors.

The determination of $\rho_\epsilon(E)$ becomes increasingly difficult for smaller smearing widths ϵ at fixed energy E, and increasing E with fixed ϵ. As evident from the right two panels of Fig. 6, it's difficult to achieve precise results outside of the elastic region for $\epsilon \lesssim m/2$ with the gaussian smearing kernel. Better is to exploit the smoothness of $\rho(E)$ and scale $\epsilon \propto (E - 2m)$, so that an equal proportion of the smearing kernel 'leaks' down to the two particle threshold at each energy.

This enables the determination of $\rho(E)$ in Fig. 9, which is the main result of this work.

The analysis performed here is (in principle) directly applicable to the vector-vector correlator in QCD to compute the R-ratio, provided a few key points are addressed. First, the presence of narrow resonances in QCD seemingly invalidates our approach to the $\epsilon \to 0$ extrapolation by scaling $\epsilon \propto (E - 2m)$. Nonetheless, the finite smearing width may be used to probe the onset of the perturbative regime [20]. Furthermore, although the density of states is higher in three spatial dimensions compared to one, the spatial extent achieved here of $mL = 30$ is currently beyond the current state of the art for simulations at physical quark masses. In this respect, the masterfield simulation paradigm [21, 22] may enable larger volumes in the near future [23].

Apart from this, the difficulty in the reconstruction problem faced here may in fact be similar to QCD. Although the use of $\tau_{\max} = 160$ may seem daunting, Fig. 3 indicates that reducing the range and density of input correlator time slices likely as little effect.Although the input correlator data for this work is generated using the two-cluster algorithm, it still possesses an exponentially degrading signal-to-noise ratio which decays at a rate empirically similar to m, as expected for the vector-vector correlator in QCD. Also, as is typical with scalar field theory, the statistical errors achieved at $C(m_\pi^{-1})$ are roughly comparable with state-of-the-art determinations of the vector-vector correlator in QCD.

Finally, the validation of the spectral reconstruction procedure presented here is intended as a stepping stone to other applications. Among them is the determination of exclusive scattering amplitudes by exploiting an asymptotic formalism as in Refs. [5, 6]. There are several additional challenges there compared to this work, including the computation and spectral reconstruction of at least three-point temporal correlation functions with two associated time separations. Nonetheless, this may provide an alternative to the finite-volume formalism for determining few-body scattering amplitudes where applicable, and extend the reach of such computations by enabling (in principle) arbitrary center-of-mass energies.

ACKNOWLEDGMENTS

We thank Martin R. Hansen for his participation at an early stage of this work and acknowledge helpful conversations with R. Sommer and P. Weisz, who also provided comments on a previous version of this manuscript. We also thank the organizers of the CERN Workshop "Advances in Lattice Gauge Theory" where work on this project began. The work of MTH is supported by UK Research and Innovation Future Leader Fellowship MR/T019956/1. The research of AP is funded by the Deutsche Forschungsgemeinschaft (DFG, German Research Foundation) - Projektnummer 417533893/GRK2575 "Rethinking Quantum Field Theory". This work was supported by CINECA that granted computing resources on the Marconi supercomputer to the LQCD123 INFN theoretical initiative under the CINECA-INFN agreement.

Appendix A: Analytic expressions for the spectral density

Thanks to the integrability of the O(3)-model, the matrix elements of the Noether current j_μ between the vacuum and a generic n-particle state (*form factors*) are completely determined by a known set of recursive functional equations, derived by Karowski and Weisz [24]. These functional equations are written in terms of the S-matrix of the system, which has been analytically derived by Zamolodchikov and Zamolodchikov [25] on the basis of the integrability of the model and some fairly weak assumptions. The n-particle contribution to the spectral function of the Noether current can be reconstructed from the form factors. This program has indeed been carried out by Balog and Niedermaier [26] for $n = 2, 4, 6$. Interestingly, the original motivation for this calculation was the calculation of the Euclidean two-point function of the O(3)-model, and the comparison with lattice simulations and perturbative calculations [27].

For the reader's convenience, we summarize here the most important formulae taken from [26]. First we need to notice that we use a different normalization for spectral density with respect to Balog and Niedermaier (BN), i.e.

$$\rho(\mu) = \frac{3\mu}{2}\,\rho_{\rm BN}(\mu) = \frac{3\mu}{2}\sum_{n=2,4,\ldots}\rho^{(n)}_{\rm BN}(\mu)\ . \tag{A1}$$

With our normalization, the large-μ behaviour of the spectral density is given by $\rho(\mu) = 1/(2\pi) + O(g^2(\mu))$.

The form factors are usually written in terms of the rapidity $\theta_{i=1,\ldots,n}$ variables. The (spatial) momentum and energy of the i-th particle are given by

$$p_i = m\sinh\theta_i\ , \qquad E_i = E(p_i) = m\cosh\theta_i\ . \tag{A2}$$

The invariant mass of a system of n particles is given by

$$M^{(n)} = \left\{\left(\sum_{i=1}^n E_i\right)^2 - \left(\sum_{i=1}^n p_i\right)^2\right\}^{1/2} = m\left\{n + 2\sum_{1\le i<j\le n}\cosh(\theta_i-\theta_j)\right\}^{1/2}\ , \tag{A3}$$

where trivial hyperbolic function relations have been used to obtain the final expression. Notably the invariant mass depends only on the rapidity differences. It turns out that it is convenient to define the new variables

$$u_{i=1,\ldots,n-1} = \theta_i - \theta_{i+1}\ . \tag{A4}$$

The kinematic of the n-particle system is completely specified by the set of variables $\theta_{i=1,\ldots,n}$, or equivalently by θ_n and $u_{i=1,\ldots,n-1}$. In terms of the new variables, we obtain in particular

$$\theta_i - \theta_j = \sum_{k=i}^{j-1} u_k\ , \qquad \text{for } 1\le i<j\le n\ . \tag{A5}$$

Once the phase-space integral appearing in the definition of the n-particle contribution to the spectral function has been written in terms of the new variables, one can use the delta function over the spatial momentum to eliminate the integral over θ_n. One is left with the integral over the variables $u_{i=1,\ldots,n-1}$ of a known functions times the delta function over the invariant mass:

$$\rho^{(n)}_{\rm BN}(\mu) = \int_0^\infty \frac{du_1\cdots du_{n-1}}{(4\pi)^{n-1}} F^{(n)}(u)\delta\left(\mu - M^{(n)}(u)\right)\ . \tag{A6}$$

The form factor is parametrized as follows

$$F^{(n)}(u) = \frac{\pi^{3n-2}}{4}G^{(n)}(u)\prod_{1\le i<j\le n}\left|\frac{\theta_{ij}-i\pi}{\theta_{ij}(2\pi i-\theta_{ij})}\tanh^2\frac{\theta_{ij}}{2}\right|_{\theta_{ij}=\theta_i-\theta_j}\ , \tag{A7}$$

where the r.h.s. can be written as a function of u by means of eq. (A5), and the functions $G^{(n)}(u)$ are polynomials in u which are explicitly written in [26] for $n = 2, 4, 6$. We report here only

$$G^{(2)}(u) = 2\ , \tag{A8}$$

$$G^{(4)}(u) = -4[6\tau_2^3 + 9\tau_3^2 + 40\tau_2\tau_4] + 8\pi^2[25\tau_2^2 + 44\tau_4] - 448\pi^2\tau_2 + 272\pi^6\ , \tag{A9}$$

where, for the $n = 4$ case, the following auxiliary variables have been introduced

$$\tau_{k=1,2,3,4} = \sum_{1\le i_1<\cdots<i_k\le 4}\prod_{\ell=1}^k\left(\theta_{i_\ell} - \frac{1}{4}\sum_{j=1}^4\theta_j\right)\ . \tag{A10}$$

The corresponding expressions for $n = 6$ are much longer, but present no logical complication. In order to calculate the integral (A6) numerically we have solved the equation $M^{(n)}(u) = \mu > 0$ for e.g. u_{n-1}. The only positive solution $\bar u_{n-1}(u_1,\ldots,u_{n-2})$ can be written explicitly by means of standard algebraic manipulations. The integral over u_{n-1} is then explicitly calculated, yielding

$$\rho^{(n)}_{\rm BN}(\mu) = \int_{M^{(n)}(u_1,\ldots,u_{n-2},0)<\mu}\frac{du_1\cdots du_{n-2}}{(4\pi)^{n-1}}\left\{\left[\frac{\partial M^{(n)}}{\partial u_{n-1}}(u)\right]^{-1}F^{(n)}(u)\right\}_{u_{n-1}=\bar u_{n-1}(u_1,\ldots,u_{n-2})}\ . \tag{A11}$$

Notice that for $n = 2$ there is no remaining integral, and one obtains the closed expression

$$\rho^{(2)}_{\rm BN}(\mu) = \theta(\mu - 2m)\frac{8\pi^3 m^5}{\mu^6}\left(\frac{\mu^2}{4m^2} - 1\right)^{5/2}\left[\frac{\bar{u}_1^2 + \pi^2}{\bar{u}_1^2(4\pi^2 + \bar{u}_1^2)}\right]_{\bar{u}_1 = 2\cosh^{-1}\frac{\mu}{2m}} . \tag{A12}$$

For $n = 4, 6$, the integral in (A11) has been equivalently replaced by

$$\int_{M^{(n)}(u_1,\ldots,u_{n-2},0)<\mu} \frac{du_1\cdots du_{n-2}}{(4\pi)^{n-1}} \longrightarrow \int_0^{\cosh^{-1}\frac{\mu^2 - n\,m}{2}} \frac{du_1\cdots du_{n-2}}{(4\pi)^{n-1}}\,\theta\left(\mu - M^{(n)}(u_1,\ldots,u_{n-2},0)\right) , \tag{A13}$$

and it has been calculated numerically for $m = 1$ (the m dependence can be trivially reintroduced by dimensional analysis) and a selection of values of μ, by means of the GNU Scientific Library implementation of Press and Farrar's MISER Monte Carlo algorithm [28]. In the region $\mu \leq 40m$, the 6-particle contribution to the spectral function is always smaller than the 0.2% of the sum of the 2- and 4-particle contributions.

Appendix B: Spectral reconstruction implementation

Explicit expressions and numerical implementation details of the spectral reconstruction algorithm are provided here for completeness. The presentation follows Ref. [1] with a slightly different notation. Additional information concerning the constraints used in this work is also provided.

By using a matrix-vector notation, the functionals of Eq. (16) can be expressed as

$$A[g] = a\left\{\boldsymbol{g}^T\cdot\boldsymbol{A}\cdot\boldsymbol{g} - 2\boldsymbol{g}^T\cdot\boldsymbol{f}\right\} + A[0] , \qquad B[g] = \boldsymbol{g}^T\cdot\boldsymbol{B}\cdot\boldsymbol{g} , \tag{B1}$$

where $\boldsymbol{g}^T = (g_1, \cdots, g_{\tau_{\rm max}})$ is the vector collecting the coefficients g_τ, $\boldsymbol{f}$ the vector with entries

$$f_\tau = \int_{E_0}^\infty d\omega\,\delta_\epsilon(E,\omega)\,b_\tau(\omega) , \tag{B2}$$

and $\boldsymbol{A}$ and $\boldsymbol{B}$ matrices with elements

$$A_{\tau\tau'} = a\int_{E_0}^\infty d\omega\,b_\tau(\omega)\,b_{\tau'}(\omega) , \qquad B_{\tau\tau'} = {\rm Cov}\left[aC(a\tau), aC(a\tau')\right] . \tag{B3}$$

Here $C(a\tau)$ is the correlator at time τ in lattice units and

$$A[0] = \int_{E_0}^\infty d\omega\,\left\{\delta_\epsilon(E,\omega)\right\}^2 . \tag{B4}$$

With these definitions the vector $\boldsymbol{g}^{\boldsymbol{\lambda}}$ that solves the minimum conditions of Eq. (17) is given by

$$\boldsymbol{g}^{\boldsymbol{\lambda}} = (1-\lambda)\boldsymbol{W}_{\boldsymbol{\lambda}}^{-\mathbf{1}}\cdot\boldsymbol{f} , \qquad \boldsymbol{W}_{\boldsymbol{\lambda}} = (1-\lambda)\boldsymbol{A} + \lambda\frac{A[0]}{a}\boldsymbol{B} , \tag{B5}$$

In Fig. 2 the minimization problem is subject to two different constraints on the reconstructed kernel. The first is detailed in Ref. [1] and forces the reconstructed and target kernels to have the same area

$$\int_{E_0}^\infty d\omega\,a\sum_{\tau=1}^{\tau_{\rm max}} g_\tau\,b_\tau(\omega) = \int_{E_0}^\infty d\omega\,\delta_\epsilon(E,\omega) . \tag{B6}$$

The second constraint enforces the reconstructed and target kernels to have the same peak value

$$a\sum_{\tau=1}^{\tau_{\rm max}} g_\tau\,b_\tau(E) = \delta_\epsilon(E,E) . \tag{B7}$$

Both constraints are represented in vector notation as

$$\boldsymbol{R}^T\cdot\boldsymbol{g} = r , \tag{B8}$$

where for the constraint in Eq. (B6) the entries of the vector $\boldsymbol{R}$ and the constant r are given by

$$R_\tau = a\int_{E_0}^{\infty} d\omega\, b_\tau(\omega)\,, \qquad r = \int_{E_0}^{\infty} d\omega\, \delta_\epsilon(E,\omega)\,, \tag{B9}$$

while for the constraint in Eq. (B7) they are given by

$$R_\tau = b_\tau(E)\,, \qquad r = \frac{\delta_\epsilon(E,E)}{a}\,. \tag{B10}$$

The solution of the minimization problem subject to Eq. (B8) is

$$\boldsymbol{g^\lambda} = (1-\lambda)\boldsymbol{W_\lambda^{-1}}\cdot\boldsymbol{f} + \boldsymbol{W_\lambda^{-1}}\cdot\boldsymbol{R}\,\frac{r-(1-\lambda)\boldsymbol{R}^T\cdot\boldsymbol{W_\lambda^{-1}}\cdot\boldsymbol{f}}{\boldsymbol{R}^T\cdot\boldsymbol{W_\lambda^{-1}}\cdot\boldsymbol{R}}\,. \tag{B11}$$

For the basis function actually used in this work, namely

$$b_{T,\tau}(E) = e^{-aE\tau} + e^{-E(T-a\tau)}\,, \tag{B12}$$

the explicit expressions for the entries of the matrix $\boldsymbol{A}$ are

$$A_{\tau\tau'} = \frac{e^{-E_0(a\tau+a\tau')}}{\tau+\tau'} + \frac{e^{-E_0(T-a\tau+a\tau')}}{T/a-\tau+\tau'} + \frac{e^{-E_0(T-a\tau'+a\tau)}}{T/a-\tau'+\tau} + \frac{e^{-E_0(2T-a\tau-a\tau')}}{2T/a-\tau-\tau'}\,. \tag{B13}$$

When $\tau_{\max}$ is large this matrix is very poorly conditioned. Consequently, when λ is small and/or the error on the correlator is small, the coefficients g_τ^λ are large in magnitude and oscillate in sign at different values of τ. In these situations, the signal on the reconstructed spectral density, given in vector notation by

$$\rho_\epsilon^\lambda(E) = \boldsymbol{c}^T\cdot\boldsymbol{g^\lambda}\,, \qquad c_\tau = aC(a\tau)\,, \tag{B14}$$

results from large numerical cancellations. For this reason (as in Ref. [1]), an implementation using extended-precision arithmetic is advocated. This is relatively straightforward for the kernels considered in this work using the libraries of Refs. [29, 30] because the integrals appearing in Eqs. (B2), (B4), and (B9) can be expressed in terms of standard special functions already implemented in these packages[8]. In the case of more generic kernels a numerical integration routine implemented in extended-precision arithmetic might be needed. An implementation based on the double-exponential quadrature algorithm [31] is available upon request.

Appendix C: Finite-volume effects in the smeared spectral function

In this appendix we present results concerning finite-volume effects in the two-particle spectral function, $\rho^{(2)}(E)$. We begin by introducing $\rho_{\infty,L,\epsilon}$ as the full spectral function at finite L and infinite T, smeared with a resolution function. This can be written as

$$\rho_{\infty,L,\epsilon}(E) = \sum_n c_n(L)\delta_\epsilon(E-E_n(L))\,, \tag{C1}$$

where $E_n(L)$ is the nth excited state $|n,L\rangle$ of the finite-volume hamiltonian with zero spatial momentum, $\delta_\epsilon(x)$ is a generic smearing kernel and

$$c_n(L) = L\sum_a \left|\langle 0|\hat{j}_1^a(0)|n,L\rangle\right|^2. \tag{C2}$$

For $E_n(L) < 4m$, one intuitively expects both the energy and the corresponding matrix element defining $c_n(L)$ to be dominated by two-particle interactions. This is made rigorous by the Lüscher quantization condition and the Lellouch-Lüscher relation which, in the present case, are given by

$$E_n(L) = Q^{-1}(\pi n) + \mathcal{O}(e^{-mL})\,, \tag{C3}$$

$$c_n(L) = \pi\left(\frac{\partial Q(E)}{\partial E}\right)^{-1}\rho^{(2)}(E)\Big|_{E=E_n(L)} + \mathcal{O}(e^{-mL})\,, \tag{C4}$$

[8] See for example the publicly available code at `https://github.com/mrlhansen/rmsd`

for

$$Q(E) \equiv \delta_{I=1}(E) + \frac{L\sqrt{E^2/4 - m^2}}{2}\,. \tag{C5}$$

This means that the values of both the energy and the overlap are dictated, up to corrections exponentially suppressed in the box length, by kinematic factors and the two-particle scattering phase shift $\delta_{I=1}(E)$. Here we include the $I = 1$ label to stress that the scattering phase corresponds to two-particle states transforming irreducibly under the fundamental representation of O(3). This label helps to distinguish the phase shift from the resolution function $\delta_\epsilon(x)$ as well as the Dirac delta function, to be used below. The quantity $\delta_{I=1}$ can be written explicitly via the analytically known S-matrix, denoted $S(k)$:

$$\delta_{I=1}(E) \equiv \frac{1}{2i}\log[S(k)]\Big|_{k=\sqrt{E^2/4-m^2}}\,, \tag{C6}$$

$$S(k) = \frac{\theta + 2i\pi}{\theta - 2i\pi}\frac{\theta - i\pi}{\theta + i\pi}\Big|_{\theta = 2\sinh^{-1}\frac{k}{m}}\,, \tag{C7}$$

where the log is defined such that $0 < \delta_{I=1}(E) < \pi$. Note that the θ used here matches that of Eq. (9), since

$$\frac{E^2}{4m^2} = 1 + \frac{k^2}{m^2} \implies \sinh^{-1}\frac{k}{m} = \cosh^{-1}\frac{E}{2m}\,. \tag{C8}$$

This leads us to define the two-particle, finite-volume, smeared spectral function as

$$\rho^{(2)}_{L,\epsilon}(E) \equiv \sum_n \pi\left(\frac{\partial Q(\omega)}{\partial\omega}\right)^{-1}\delta_\epsilon(E-\omega)\rho^{(2)}(\omega)\Big|_{\omega = Q^{-1}(\pi n)}\,, \tag{C9}$$

where we have dropped the $T = \infty$ label. If $\delta_\epsilon(x)$ has compact support and ϵ and E are chosen so that only $E_n(L) < 4m$ states contribute, then this corresponds to the smeared finite-volume spectral function defined in Eq. (C1). By contrast, for non-compact smearing or for $E > 4m$, $\rho^{(2)}_{L,\epsilon}$ represents an approximation of the full, smeared finite-volume spectral function in which the role of infinite-volume states with more than two-particles is ignored.

In the remainder of this appendix, we study $\rho^{(2)}_{L,\epsilon}(E)$ as defined and show that terms scaling as $1/L$ cancel in this quantity, provided that $\delta_\epsilon(x)$ is differentiable and falls off fast enough as $x \to \infty$. The precise condition is given after Eq. (C19) below. We additionally show a stronger result, that $\rho^{(2)}_{L,\epsilon}(E)$ has exponentially suppressed volume effects, provided $\delta_\epsilon(x)$ is analytic in some finite-width strip about the real axis. Before investigating the nature of the scaling at asymptotically large L, we warm up by formally evaluating the $L \to \infty$ limit of Eq. (C9)

$$\rho^{(2)}_{\infty,\epsilon}(E) \equiv \lim_{L\to\infty}\rho^{(2)}_{L,\epsilon}(E)\,, \tag{C10}$$

$$= \lim_{L\to\infty}\frac{1}{L}\sum_n \pi\left(\frac{1}{2}\frac{\partial\sqrt{\omega^2/4-m^2}}{\partial\omega} + \frac{1}{L}\frac{\partial\delta_{I=1}(\omega)}{\partial\omega}\right)^{-1}\delta_\epsilon(E-\omega)\rho^{(2)}(\omega)\Big|_{\omega=Q^{-1}(\pi n)}\,, \tag{C11}$$

$$= \int_0^\infty \frac{dk}{2\pi}\,\pi\left(\frac{1}{2}\frac{\partial\sqrt{\omega^2/4-m^2}}{\partial\omega}\right)^{-1}\delta_\epsilon(E-\omega)\rho^{(2)}(\omega)\Big|_{\omega=2\sqrt{m^2+k^2}}\,, \tag{C12}$$

where in the final line we have dropped contributions to the finite-volume energy and the Lellouch-Lüscher factor that are $1/L$ suppressed, replaced the sum over n with an integral and performed the change of variables $k = 2\pi n/L$. These results hold for any smearing function $\delta_\epsilon(x)$ for which the integral converges. Finally, changing integration variables to ω, we deduce

$$\rho^{(2)}_{\infty,\epsilon}(E) = \int_{2m}^\infty d\omega\,\delta_\epsilon(E-\omega)\rho^{(2)}(\omega)\,, \tag{C13}$$

as expected.

1. $1/L$ cancellation

We are ready to show that the $1/L$ contributions appearing within the finite-volume energies and Lellouch-Lüscher factors cancel in the definition of $\rho^{(2)}_{L,\epsilon}(E)$. First write

$$\rho^{(2)}_{L,\epsilon}(E) = \rho^{(2)}_{\infty,\epsilon}(E) + \frac{c^{(1)}(E)}{L} + \mathcal{O}(1/L^2)\,, \tag{C14}$$

implying

$$c^{(1)}(E) \equiv \lim_{L\to\infty} L\big[\rho^{(2)}_{L,\epsilon}(E) - \rho^{(2)}_{\infty,\epsilon}(E)\big]\,. \tag{C15}$$

Contributions to this coefficient arise from the leading-order shift to both the matrix element and the energy. The former can be written as

$$\left(\frac{\partial Q(\omega)}{\partial\omega}\right)^{-1} = \frac{1}{L}\frac{8k}{\omega}\left[1 - \frac{1}{L}\frac{8k}{\omega}\frac{\partial\delta_{I=1}(\omega)}{\partial\omega}\right] + \mathcal{O}(1/L^3)\,, \tag{C16}$$

where we have substituted $\partial k/\partial\omega = \omega/(4k)$ for $k = \sqrt{\omega^2/4 - m^2}$. The corresponding result for the energy can be found by expanding Eq. (C3)

$$E_n(L) = 2\sqrt{m^2 + k^2} - \frac{1}{L}\frac{8k}{\omega}\delta_{I=1}(\omega) + \mathcal{O}(1/L^2)\,, \tag{C17}$$

where here $k = 2\pi n/L$.

Putting everything together, we reach

$$c^{(1)}(E) = -\lim_{L\to\infty}\frac{1}{L}\sum_n \pi\frac{8k}{\omega}\left(\delta_{I=1}(\omega)\frac{\partial}{\partial\omega} + \frac{\partial\delta_{I=1}(\omega)}{\partial\omega}\right)\frac{8k}{\omega}\delta_\epsilon(E-\omega)\rho^{(2)}(\omega)\bigg|_{\omega=2\sqrt{m^2+k^2}}\,, \tag{C18}$$

where the first term in parenthesis arises from the energy shift and the second from the matrix element. Evaluating the limit, we deduce

$$c^{(1)}(E) = -\int_{2m}^{\infty} d\omega\,\frac{d}{d\omega}\left[\delta_{I=1}(\omega)\frac{8\sqrt{\omega^2/4 - m^2}}{\omega}\delta_\epsilon(E-\omega)\rho^{(2)}(\omega)\right]. \tag{C19}$$

Thus, the precise condition on $\delta_\epsilon(x)$ is that the integral above should vanish. This holds as long as the full integrand is Riemann integrable and the quantity in square brackets vanishes at $\omega = 2m$ and as $\omega \to \infty$. All the smearing functions considered in this work satisfy this condition as do much more aggressive choices, e.g. taking $\delta_\epsilon(x)$ as a a function with compact support in the region $[x-\epsilon, x+\epsilon]$ that vanishes on both sides of the indicated window.

2. Exponentially suppressed volume effects

We now demonstrate that, for a more restrictive class of smearing functions, the volume effects are in fact exponentially suppressed in the box length. This result also holds for all of the smearing functions used in this work. The argument is based on an elegant identity that is closely related to the derivation of the Lellouch-Lüscher formalism. One can combine the appearance of $(\partial Q(\omega)/\partial\omega)$ with the definition of the finite-volume energies to re-write Eq. (C9) as

$$\rho^{(2)}_{L,\epsilon}(E) \equiv 2\pi\int_{2m}^{\infty} d\omega\;\delta_\epsilon(E-\omega)\;\sum_{n=0}^{\infty}\delta\big(2Q(\omega) - 2\pi n\big)\rho^{(2)}(\omega)\,, \tag{C20}$$

where the delta without the ϵ subscript is the standard Dirac delta function. The relation $\delta\big(f(x)\big) = |f'(x)|^{-1}\delta(x)$ can be used to show that this expression is equivalent to Eq. (C9).

Next we use that $Q(E)$ is non-negative[9] to extend the sum over n to include all integers. Then applying the Poisson summation formula

$$\sum_{n=-\infty}^{\infty}\delta(x - 2\pi n) = \frac{1}{2\pi}\sum_{n=-\infty}^{\infty} e^{inx}\,, \tag{C21}$$

[9] This holds for the positive $I = 1$ phase shift for all L values, whereas for systems with negative scattering phase shift $Q(E) > 0$ is only guaranteed above some sufficiently large value of L.

we deduce

$$\rho^{(2)}_{L,\epsilon}(E) = \sum_{n=-\infty}^{\infty} \int_{2m}^{\infty} d\omega\, \delta_\epsilon(E-\omega)\, e^{i2nQ(\omega)} \rho^{(2)}(\omega)\,, \tag{C22}$$

$$= \sum_{n=-\infty}^{\infty} \int_{2m}^{\infty} d\omega\, \delta_\epsilon(E-\omega)\, e^{inLk} [S(k)]^n \rho^{(2)}(\omega)\,, \tag{C23}$$

where in the second line we have substituted the definition of $Q(E)$, Eq. (C5). Now taking the expressions for the spectral function and S-matrix, Eqs. (9) and (C7) respectively, we reach

$$\rho^{(2)}_{L,\epsilon}(E) = \frac{3\pi^3}{4} \sum_{n=-\infty}^{\infty} \int_{0}^{\infty} dk\, \delta_\epsilon(E-\omega)\, e^{inLk}\, \mathcal{I}_n(\theta)\,, \tag{C24}$$

$$\mathcal{I}_n(\theta) \equiv \left[\frac{\theta+2i\pi}{\theta-2i\pi}\frac{\theta-i\pi}{\theta+i\pi}\right]^n \frac{1}{\theta^2}\,\frac{\theta^2+\pi^2}{\theta^2+4\pi^2}\,\tanh^4\frac{\theta}{2}\,, \tag{C25}$$

where, as above, $\theta = 2\sinh^{-1}(k/m)$ and $\omega = 2\sqrt{k^2+m^2}$. Note that the integrand here has an additional factor of $\tanh(\theta/2)$, arising from the Jacobian in the change of integration variable: $\partial\omega/\partial k = 2k/\sqrt{k^2+m^2} = 2\tanh(\theta/2)$.

This explicit form of the integral is useful for two reasons: First, it makes manifest that the integrand is invariant under the simultaneous replacements $n \to -n$ and $k \to -k$ ($\theta \to -\theta$). Second, it exhibits the analytic structure of the integrand as a function of k. In particular, if $\delta_\epsilon(x)$ is an analytic function of its argument, then the integrand is an analytic function of k, in a strip of width $2m$ centered on and running along the real k axis. The non-analyticity arises from $\omega = 2\sqrt{k^2+m^2}$ within $\delta_\epsilon(E-\omega)$ as well as the S-matrix (in square brackets) and $\tanh(\theta/2)$. The latter factors have poles when $\theta = \pm i\pi$ corresponding to $k = \pm im$. Note also that the $\tanh^4(\theta/2)$ factor cancels the apparent $1/\theta^2$ singularity.

From these two observations, it follows that one can extend the range of integration in k along the entire real axis and then shift the integration contour to $\mathbb{R} + i\mu$, where μ is either the mass m or (if it is less than m) the imaginary part of the nearest singularity in k resulting from $\delta_\epsilon(E-\omega)$. Concerning the kernels used in this work, $\mu = m$ always holds for the Gaussian kernel `g` but for the Cauchy kernels, `c0`, `c1` and `c2`, the singularity at $(E-2\sqrt{m^2+k^2})^2 = -\epsilon^2$ can be a distance less than m from the real axis. In this case one has

$$\mu = \mathrm{Im}\sqrt{\frac{E^2-4m^2-\epsilon^2}{4} + \frac{iE\epsilon}{2}} = \frac{\epsilon}{2}\left[1 + \frac{2m^2}{E^2} + \frac{2m^2(3m^2-\epsilon^2)}{E^4} + O(1/E^6)\right], \tag{C26}$$

where the large E expansion gives an indicator of the values that might be realized. We have also explicitly checked that the contributions from the vertical segments $\pm\infty$ to $\pm\infty + i\mu$ vanish for any smearing function that vanishes as $k \to \infty$.

Extending the integration range and shifting the contour in Eq. (C24) as described, we find that the difference between finite- and infinite-volume smeared spectral functions can be written as

$$\Delta\rho^{(2)}_{L,\epsilon}(E) \equiv \rho^{(2)}_{L,\epsilon}(E) - \rho^{(2)}_{\infty,\epsilon}(E) = \sum_{n=1}^{\infty} \mathcal{C}_n(E,L,\mu) e^{-n\mu L}\,, \tag{C27}$$

The coefficient $\mathcal{C}_n$ is oscillatory with an envelope that is either constant or falling with a power of L and is defined via

$$\mathcal{C}_n(E,L,\mu) \equiv \frac{3\pi^3}{8} \lim_{\eta\to\mu^-} \mathrm{Re} \int_{-\infty}^{\infty} dx\, \delta_\epsilon(E-\omega_\eta(x))\, e^{inLx}\, \mathcal{I}_n(\theta_\eta(x))\,, \tag{C28}$$

with $\theta_\eta(x) = 2\sinh^{-1}[(x+i\eta)/m]$ and $\omega_\eta(x) = 2\sqrt{(x+i\eta)^2+m^2}$.

We have also studied these results numerically and confirmed that the straightforward expression based on a sum over finite-volume states, Eq. (C9), matches the sum over Poisson modes, evaluated both with the original contour (Eq. (C24)) and the shifted contour that makes the $e^{-\mu L}$ scaling manifest (Eq. (C27)). In Fig. 10 we show the results for the Gaussian kernel, plotted as a function of E at fixed ϵ and L. In Fig. 11 we plot $\Delta\rho^{(2)}_{L,\epsilon}(E)$ at fixed E and ϵ versus L for both the Gaussian and Cauchy kernels. We see that the volume effects are oscillatory functions of L with an envelope decaying according to the predicted exponential.

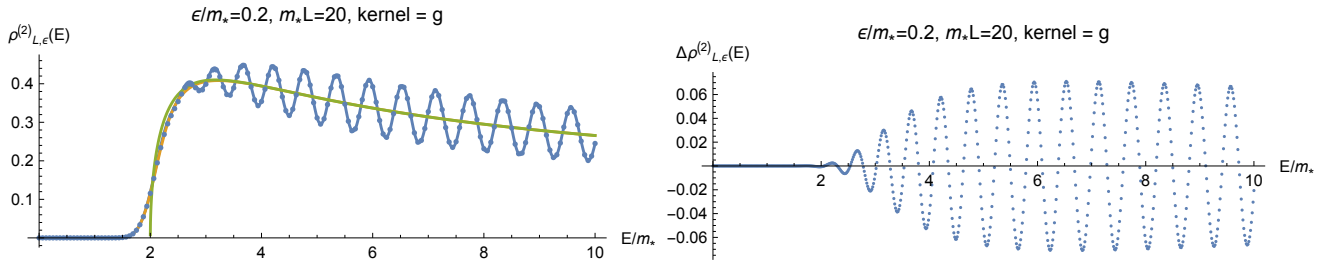

FIG. 10. **Left:** Plot of theoretically predicted two-particle spectral functions vs. E, including the unsmeared and smeared infinite-volume results, as well as the finite-volume smeared spectral function defined in Eq. (C9). The points arise from numerically evaluating the $n = 1$ term of Eq. (C27) and combining with $\rho_{\infty,\epsilon}(E)$. **Right:** Direct evaluation of the $n = 1$ contribution to the residue, Eq. (C27). We have confirmed that the effect of the e^{-2mL} term is highly suppressed and cannot be resolved on these plots. Plots to be beautified and legend to be included. Star to be discarded.

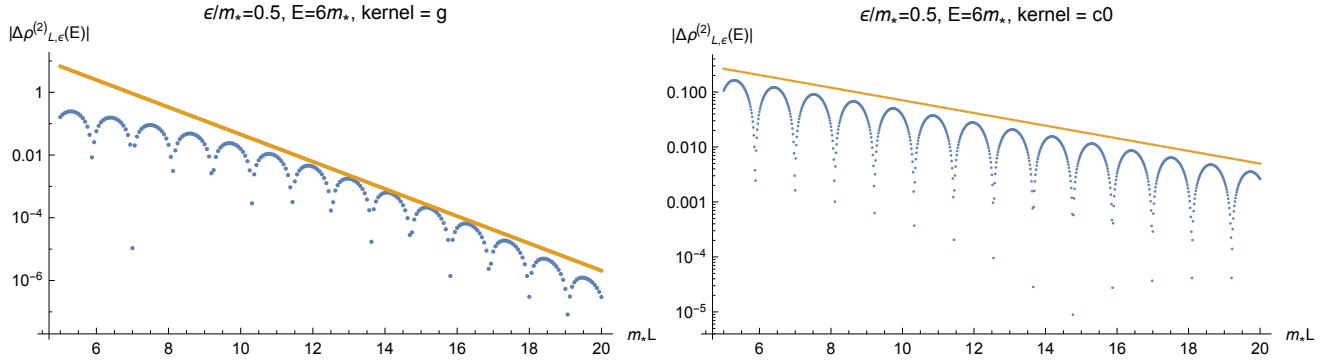

FIG. 11. Plots of the finite-volume residue vs. L for the Gaussian kernel (g, left) and Cauchy kernel (c0, right). The orange curves give the predicted $e^{-\mu L}$ scaling for each; $\mu = m$ for the Gaussian and $\mu = 0.265m$ for the Cauchy, slightly exceeding $\epsilon/2$ as given by Eq. (C26). Plots to be beautified and legend to be included.

Appendix D: Simulation algorithm

We employ the single-cluster algorithm and associated cluster estimators from Ref. [12] which are briefly summarized here. A cluster update proceeds as follows. First, a random vector $r \in \mathbb{R}^3$, $|r| = 1$ is drawn uniformly from the unit sphere. Then a 'seed' site is chosen uniformly as the first member of the cluster. For each new site x added to the cluster, consider all non-cluster sites among the four nearest neighbors of x. A neighbor y is added to the cluster with probability

$$p_{\text{add}} = 1 - \exp\left[\min\{-2\beta\sigma_r(x)\sigma_r(y), 0\}\right] \tag{D1}$$

where $\sigma_r(x) = \sigma(x) \cdot r$. After all cluster neighbors have been considered for addition, all cluster sites are updated according to

$$\sigma^a(x) \to \sigma^a(x) - 2\sigma_r(x)r^a. \tag{D2}$$

In order to employ a cluster estimator for $C(a\tau)$, which contains four fundamental fields, a second orthogonal cluster update is required. This proceeds by choosing a second random vector u from the unit sphere with the constraint that $r \cdot u = 0$. This second cluster update then proceeds in the same manner. The combination of a single r-update followed by a u-update is henceforth referred to as a 'cluster update', the number of which are tabulated in Tab. II for each ensemble.

The cluster estimator for $C(a\tau)$ is built from

$$\tilde{\sigma}_{r,u}(x) = \sqrt{\frac{|\Lambda|}{N_{r,u}}}\theta_{r,u}(x)\sigma_{r,u}(x) \tag{D3}$$

where $N_{r,u}/|\Lambda|$ is the cluster fraction and $\theta_{r,u}(x)$ the characteristic function. Expectation values $\langle\ldots\rangle_{1\text{C}}$ denote integration over all possible pairs of orthogonal single-cluster configurations as well as the usual integration over the

field variables. Straightforward application of Eq. (37) gives

$$\langle j^a_\mu(x) j^a_\mu(y)\rangle = 2\beta^2\, P(ab|cd)\,\langle \sigma_a(x)\sigma_b(x+a\hat{\mu})\sigma_c(y)\sigma_d(y+a\hat{\mu})\rangle = 12\beta^2\,\langle \tilde{\sigma}_{[r}(x)\tilde{\sigma}_{u]}(x+a\hat{\mu})\,\tilde{\sigma}_{[r}(y)\sigma_{u]}(y+a\hat{\mu})\rangle_{1\mathrm{C}} \quad \text{(D4)}$$

where $P(ab|cd) = \frac{1}{2}(\delta_{ac}\delta_{bd} - \delta_{ad}\delta_{bc})$ and $\tilde{\sigma}_{[r}(x)\tilde{\sigma}_{u]}(y) = \frac{1}{2}\{\tilde{\sigma}_r(x)\tilde{\sigma}_u(y) - \tilde{\sigma}_u(x)\tilde{\sigma}_r(y)\}$. The correlator is then given by

$$C(a\tau) = \frac{12\beta^2}{L/a}\langle \Phi_{ru}(a\tau)\,\Phi_{ru}(0)\rangle_{1\mathrm{C}}, \qquad \Phi_{ru}(a\tau) = \sum_{\boldsymbol{x}} \tilde{\sigma}_{[r}(a\tau,\boldsymbol{x})\tilde{\sigma}_{u]}(a\tau,\boldsymbol{x}+a\hat{1})\,, \quad \text{(D5)}$$

where (although not denoted explicitly) time translation invariance is employed to average over all equivalent time separations on the periodic torus.

The estimator for $C(a\tau)$ in Eq. (D5) is not positive definite, in contrast to the cluster estimator for the two-point function of the fundamental fields, which requires only a single cluster. The computational cost of $\Phi_{ru}(a\tau)$ for a single update scales only weakly with the lattice size at fixed β, since only pairs of sites which are neighbors in the spatial direction and belong to different clusters contribute. However this overlap becomes increasingly unlikely, resulting in an increasing statistical error for a fixed number of cluster updates. Despite this 'cluster cutoff', the variance of the estimator in Eq. (D5) decays exponentially with increasing τ, while the one for standard estimator (given by the middle expression in Eq. (D4)) approaches a constant. The cluster estimator thus results in a significant improvement in the signal-to-noise ratio, which empirically decays with a rate roughly similar to m.

[1] M. Hansen, A. Lupo, and N. Tantalo, *Extraction of spectral densities from lattice correlators*, *Phys. Rev.* **D99** (2019), no. 9 094508, [arXiv:1903.06476].

[2] M. Lüscher, *Two particle states on a torus and their relation to the scattering matrix*, *Nucl. Phys.* **B354** (1991) 531–578.

[3] J. C. A. Barata and K. Fredenhagen, *Particle scattering in Euclidean lattice field theories*, *Commun. Math. Phys.* **138** (1991) 507–520.

[4] M. T. Hansen, H. B. Meyer, and D. Robaina, *From deep inelastic scattering to heavy-flavor semileptonic decays: Total rates into multihadron final states from lattice QCD*, *Phys. Rev.* **D96** (2017), no. 9 094513, [arXiv:1704.08993].

[5] J. Bulava and M. T. Hansen, *Scattering amplitudes from finite-volume spectral functions*, *Phys. Rev.* **D100** (2019), no. 3 034521, [arXiv:1903.11735].

[6] M. Bruno and M. T. Hansen, *Variations on the Maiani-Testa approach and the inverse problem*, arXiv:2012.11488.

[7] S. Hashimoto, *Inclusive semi-leptonic B meson decay structure functions from lattice QCD*, *PTEP* **2017** (2017), no. 5 053B03, [arXiv:1703.01881].

[8] P. Gambino and S. Hashimoto, *Inclusive Semileptonic Decays from Lattice QCD*, *Phys. Rev. Lett.* **125** (2020), no. 3 032001, [arXiv:2005.13730].

[9] G. Backus and F. Gilbert, *The resolving power of gross earth data*, *Geophysical Journal International* **16** (1968), no. 2 169–205.

[10] G. Backus and F. Gilbert, *Uniqueness in the inversion of inaccurate gross earth data*, *Philosophical Transactions of the Royal Society of London A: Mathematical, Physical and Engineering Sciences* **266** (1970), no. 1173 123–192, [http://rsta.royalsocietypublishing.org/content/266/1173/123.full.pdf].

[11] F. Pijpers and M. Thompson, *Faster formulations of the optimally localized averages method for helioseismic inversions*, *Astronomy and Astrophysics* **262** (08, 1992) L33–L36.

[12] M. Luscher and U. Wolff, *How to Calculate the Elastic Scattering Matrix in Two-dimensional Quantum Field Theories by Numerical Simulation*, *Nucl. Phys.* **B339** (1990) 222–252.

[13] P. Sabatier, ed., *Inverse Methods in Action*. Springer Verlag, 1990.

[14] L. Lellouch and M. Lüscher, *Weak transition matrix elements from finite volume correlation functions*, *Commun. Math. Phys.* **219** (2001) 31–44, [hep-lat/0003023].

[15] H. B. Meyer, *Lattice QCD and the Timelike Pion Form Factor*, *Phys. Rev. Lett.* **107** (2011) 072002, [arXiv:1105.1892].

[16] A. Francis, G. von Hippel, H. B. Meyer, and F. Jegerlehner, *Vector correlator and scale determination in lattice QCD*, *PoS* **LATTICE2013** (2013) 320, [arXiv:1312.0035].

[17] M. Hasenbusch, P. Hasenfratz, F. Niedermayer, B. Seefeld, and U. Wolff, *Nonstandard cutoff effects in the nonlinear sigma model*, *Nucl. Phys. B Proc. Suppl.* **106** (2002) 911–913, [hep-lat/0110202].

[18] J. Balog, F. Niedermayer, and P. Weisz, *Logarithmic corrections to O(a**2) lattice artifacts*, *Phys. Lett. B* **676** (2009) 188–192, [arXiv:0901.4033].

[19] J. Balog, F. Niedermayer, and P. Weisz, *The Puzzle of apparent linear lattice artifacts in the 2d non-linear sigma-model and Symanzik's solution*, *Nucl. Phys. B* **824** (2010) 563–615, [arXiv:0905.1730].

[20] E. C. Poggio, H. R. Quinn, and S. Weinberg, *Smearing the Quark Model*, *Phys. Rev. D* **13** (1976) 1958.

[21] A. Francis, P. Fritzsch, M. Lüscher, and A. Rago, *Master-field simulations of O(a)-improved lattice QCD: Algorithms, stability and exactness*, *Comput. Phys. Commun.* **255** (2020) 107355, [arXiv:1911.04533].

[22] L. Giusti and M. Lüscher, *Topological susceptibility at $T > T_c$ from master-field simulations of the SU(3) gauge theory*, *Eur. Phys. J. C* **79** (2019), no. 3 207, [arXiv:1812.02062].

[23] M. Cè, M. Bruno, J. Bulava, A. Francis, P. Fritzsch, J. R. Green, M. T. Hansen, and A. Rago, *Approaching the master-field: Hadronic observables in large volumes*, in *38th International Symposium on Lattice Field Theory*, 10, 2021. arXiv:2110.15375.

[24] M. Karowski and P. Weisz, *Exact Form-Factors in (1+1)-Dimensional Field Theoretic Models with Soliton Behavior*, *Nucl. Phys. B* **139** (1978) 455–476.

[25] A. B. Zamolodchikov and A. B. Zamolodchikov, *Relativistic Factorized S Matrix in Two-Dimensions Having O(N) Isotopic Symmetry*, *Nucl. Phys.* **B133** (1978) 525. [JETP Lett.26,457(1977)].

[26] J. Balog and M. Niedermaier, *Off-shell dynamics of the O(3) NLS model beyond Monte Carlo and perturbation theory*, *Nucl. Phys. B* **500** (1997) 421–461, [hep-th/9612039].

[27] J. Balog, M. Niedermaier, and T. Hauer, *Perturbative versus nonperturbative QFT: Lessons from the O(3) NLS model*, *Phys. Lett. B* **386** (1996) 224–232, [hep-th/9604161].

[28] W. H. Press and G. R. Farrar, *Recursive stratified sampling for multidimensional monte carlo integration*, *Computers in Physics* **4** (1990), no. 2 190–195, [https://aip.scitation.org/doi/pdf/10.1063/1.4822899].

[29] F. Johansson, *Arb: efficient arbitrary-precision midpoint-radius interval arithmetic*, *IEEE Transactions on Computers* **66** (2017) 1281–1292.

[30] L. Fousse, G. Hanrot, V. Lefèvre, P. Pélissier, and P. Zimmermann, *Mpfr: A multiple-precision binary floating-point library with correct rounding*, *ACM Trans. Math. Softw.* **33** (June, 2007) 13¿es.

[31] M. Mori and M. Sugihara, *The double-exponential transformation in numerical analysis*, *Journal of Computational and Applied Mathematics* **127** (2001), no. 1 287–296. Numerical Analysis 2000. Vol. V: Quadrature and Orthogonal Polynomials.